AECOM Imagine it. Delivered.

Offshore probabilistic tsunami hazard Puerto Rico

Version 0.1

Prepared for:

Prepared by:

Hong Kie Thio Principal Seismologist T: 213.996.2250 E: hong.kie.thio@aecom.com AECOM One California Plaza 300 South Grand Avenue Los Angeles, CA 90071 T: +1 (213) 593 8100 F: +1 (213) 593 8178 aecom.com	Elizabeth Vanacore Research Associate Department of Geology University of Puerto Rico, Mayaguez

Table of Contents

Figures

Tables

1 Introduction

This report presents the methodology, source characterization, and offshore probabilistic hazard for Puerto Rico following procedures consistent with the ASCE 7-22 guidelines. The offshore hazard can serve as an anchor point to constrain high-resolution inundation studies suitable for building code and other applications. Conform ASCE 7-22, we will calculate the hazard for a dense collection of offshore points off Puerto Rico at the 100m contour, using a reciprocal Green's function method considering sources in the Caribbean region.

The current model is based on earlier work by AECOM in the area, as well as the USGS Powell center workshops (Ross et al., 2022) on tsunami sources. Due to timing issues, the updated (2024) USGS NSHM model has not been included in this report, but will be considered as it becomes available.

The software, manual, input and output presented in this report will be made available online for further use by UPRM staff.

.

2 Probabilistic Tsunami Hazard Analysis

2.1 General Approach

Probabilistic Tsunami Hazard Analysis (PTHA) is a technique to compute the probability that a certain tsunami-related parameter (waveheight, flow velocity, etc.) is exceeded. This probability is computed based on our current understanding of the physical processes that lead to the hazard including uncertainties and variations in the source excitation of the tsunami and the propagation of the tsunami towards the site of interest.

Because of the highly non-linear character of tsunami inundation, and its high computational cost, we have developed a two-step approach to the tsunami hazard analysis at the site. In the first step, we compute a comprehensive probabilistic tsunami hazard analysis for an offshore location near the site, making use of the linear behavior of tsunami in deep water. Next, we use a source disaggregation to select one or more dominant sources and compute fully non-linear inundation models for these sources, scaled up or down to match the offshore exceedance amplitude computed in the first step.

The methodology behind the seismic equivalent, Probabilistic Seismic Hazard Analysis (PSHA) is well known (e.g., McGuire, 2004), and here we will only briefly describe the adaptations that are made for PTHA. Whereas in PSHA we are usually interested in the exceedance of some ground motion measure such as peak ground acceleration (PGA) or spectral acceleration (SA), in PTHA a parameter of interest (not necessarily the only one) is the maximum tsunami amplitude that is expected to be exceeded at sites along the coast.

The earthquake recurrence models behind the two methods are the same (Figure 2-1). The difference lies in the process that relates the occurrence of an earthquake with certain magnitude and location to the hazard at the site, such as the Ground Motion Prediction Equations (GMPE) in PSHA. In the empirically derived GMPE, this relationship is a simple function of magnitude and distance, with some corrections applied for source and site characteristics. Because of the aforementioned strong laterally varying nature of tsunami propagation, we have adopted a waveform excitation and propagation approach instead of trying to develop analogous tsunami prediction equations. In fact, current developments in PSHA include the replacement of the GMPEs with ensembles of numerically generated ground motions, which is analogous to the approach proposed here.

The excitation and propagation of tsunamis in deeper water can be modeled using the shallow water wave approximation, which is linear for amplitudes that are significantly smaller than the water depth. We can solve the equation of motion numerically using a finite-difference method, which has been validated to produce accurate tsunami heights for propagation through the oceans, although for very shallow water the amplitudes may become too large, and more sophisticated nonlinear methods are required to model the details of the run-up accurately. Nevertheless, the linear approach provides a very good first approximation of tsunami propagation, taking into account the effects of lateral variations in seafloor depth.

The procedure followed here is similar to the one used for the development of the Tsunami Design Maps that have been introduced in the American Society of Civil Engineer's ASCE 7-16 standard "Minimum Design Loads for Buildings and Other Structures" (ASCE, 2017; Thio et al., 2017).

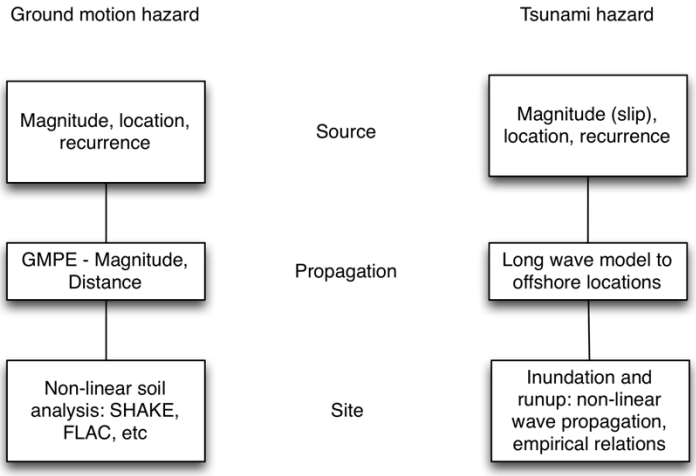

Figure 2-1 Schematic comparison between PSHA and PTHA

2.2 Epistemic uncertainty and aleatory variability

An inherent element of a probabilistic analysis is the accounting for limits to our ability of predicting natural processes, either because of a lack of knowledge, referred to as epistemic uncertainty, or because of the random nature of these processes (aleatory variability).

2.2.1 Epistemic uncertainty

Probabilistic tsunami hazard analysis, like its seismic counterpart, follows a dualistic approach to probability. Whereas some aspects are defined in the familiar terms of frequency of occurrence (such as intermediate earthquake recurrence, magnitude distribution), others are more based on judgment, which is a subjective approach (Vick, 2002). For instance, we may characterize the recurrence of intermediate earthquakes in terms of a Gutenberg-Richter distribution, constrained by a catalog of historical earthquakes. The assumption is that the occurrence of earthquakes is a stationary process, and that the catalog represents a homogenous sample of the long-term seismic behavior of a source. For large earthquakes however, the return times are often so long relative to our historic record, even when paleo-seismic data is included, that the recurrence properties of these events cannot be described with a stationary model based on a regression of observed earthquake occurrence. We therefore need to introduce the concept of judgment, where we use our current understanding of earthquake processes, including analyses of similar structures elsewhere, such as local geological conditions, fault geometry, strain rates etc., to make assumptions on the recurrence and scaling (Figure 2-2) of large earthquakes. This is a subjective or epistemic approach to probability, centered on the observer rather than the observations, and will inevitably be different from one practitioner to another. A rigorous PTHA model therefore includes the use of logic trees to express alternative understandings of the same process, e.g. large earthquake recurrence models, weighted by the subjective likelihood of that alternative model (“degree of belief”), where the weights of the alternatives sum to unity.

2.2.2 Aleatory variability

All aspects of earthquake occurrence and effects contain a measure of natural randomness, even if certain average behavior and measures are clearly identified. This variability is usually expressed in terms of distribution functions around the mean and are included in a PTHA by sampling or integrating over this distribution function (Figure 2-2). More details on the aleatory variability are discussed in the sections on the various components that contribute to the PTHA.

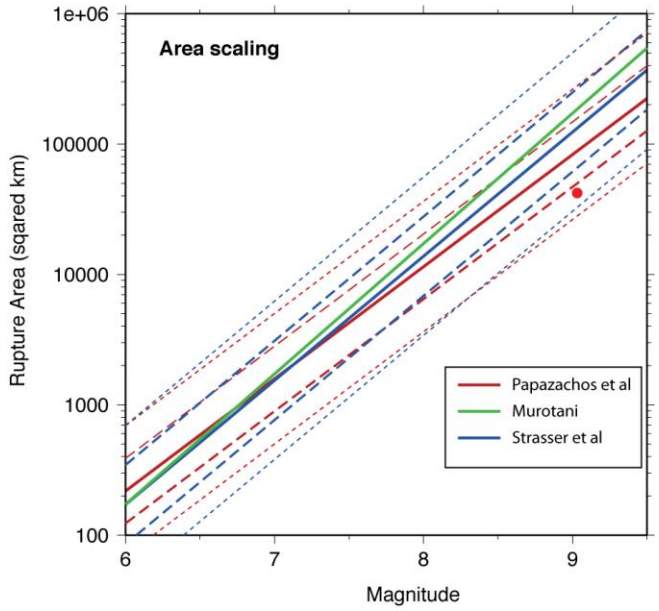

Figure 2-2 Area magnitude scaling relations. Different colors represent different scaling relations (epistemic). Dashed lines are 1 sigma, dotted lines are 2 sigma levels (aleatory). The red dot represents the 2011 Tohoku earthquake.

3 Tsunami model

3.1 Green's Function Summation

The underlying principle for this approach is the validity of the linear behavior of tsunami waves in deeper water. This enables us to deconstruct a tsunami that is generated by an earthquake into a sum of individual tsunami waveforms (Green's functions) from a set of subfaults that adequately describe the complexities in earthquake rupture. By pre-computing and storing the tsunami waveforms at points along the coast generated by each subfault for a unit slip, we can efficiently synthesize tsunami waveforms for any slip distribution by summing the individual subfault tsunami waveforms weighted by their slip. The same principle is used in the inversion of tsunami waves for earthquake rupture. This efficiency makes it feasible to use Green's function summation in lieu of attenuation relations to provide very accurate estimates of tsunami amplitude for probabilistic calculations, where one typically needs to compute thousands of earthquake scenarios. For instance, once the Green's functions were computed, the probabilistic tsunami amplitude results in this report for which we integrated over more than 10,000 scenarios, were computed on a single 24-core computer in a few hours.

The assumption of linearity is not valid for tsunamis where the amplitudes are comparable to the water depth. Also, the detailed bathymetry near the shoreline is needed to accurately estimate the final run-up heights. Therefore, we have computed the offshore Green's functions at a target depth of 100 m, which usually is a good compromise between stable computations and distance to the target site. Also, since we are computing hazard at a localized site, we used the reciprocal Green's function approach (Loomis, 1979) where the response at a site from large source areas is represented by computing the impulse response for a source at the site throughout the area.

3.2 Tsunami modeling

Contrary to traditional seismic practice, the actual propagation term in the hazard equation for tsunamis is solved using numerical models rather than empirical relationships. This is due to: (1) the very strong lateral heterogeneity in the propagating medium (the oceans) which limits the usefulness for simple empirical relationships; and (2) the greater accuracy in tsunami modeling compared to high-frequency seismic modeling. All tsunami simulation algorithms use the same initial condition, namely the vertical deformation, whether instantaneous or distributed over time, of the sea surface. This deformation is set equal to the deformation of the underlying seafloor.

3.2.1 Linear long-wave finite difference method

This method is very efficient and accurate for ocean-wide propagation but does not model inundation or non-linear effects such as bottom friction. We have used this algorithm to compute the fundamental Green's functions at the offshore location where we computed the probabilistic offshore exceedance amplitudes. For this part of the project, we used the code Comcot by Liu et al. (1995). Since we are using this code for offshore wave heights, we have not activated the non-linear and inundation components of the code.

3.2.2 Seafloor Deformation

In order to generate tsunamis from earthquake slip distributed on a fault, we need to compute the surface deformation from the slip. There are several methods available to accomplish this. The most commonly used is the analytical method of Okada (1992), which gives the surface deformation due to uniform slip on a rectangular fault in an elastically homogeneous half-space. However, Savage (1987, 1998) demonstrated that using a half-space approximation gives relatively large bias compared to a layered (1-D) model. The difference between 1-D and even

more realistic 3-D models (Wald and Graves, 2001) is much smaller, and we therefore used a 1-D frequency-wavenumber integration (FK) technique (Wang et al., 2003, 2006) to compute the static deformation at the surface.

The elastic deformation due to slip on a fault is linear, and we can use this principle to efficiently compute the vertical deformation at the surface by pre-computing the surface deformation from the elementary subfaults, after which we can reproduce surface deformation from arbitrary slip distributions by a weighted sum (weighted according to slip) of the individual contributions of each subfault.

3.3 Bathymetry

Since we are only computing tsunami waves in the offshore domain, we have used the global GEBCO model (15 arcsec) for all computations. The computation domain and the relevant sources are shown in Figure 3-1. A more detailed map around Puerto Rico and the Virgin Islands, giving a better view of the local faults, is shown in Figure 3-2. To compute the linear Green's functions, we capped the bathymetry at a depth of 10m, meaning that all areas shallower than 10m were made to 0m, so as to prevent potential destabilizing amplitude spikes.

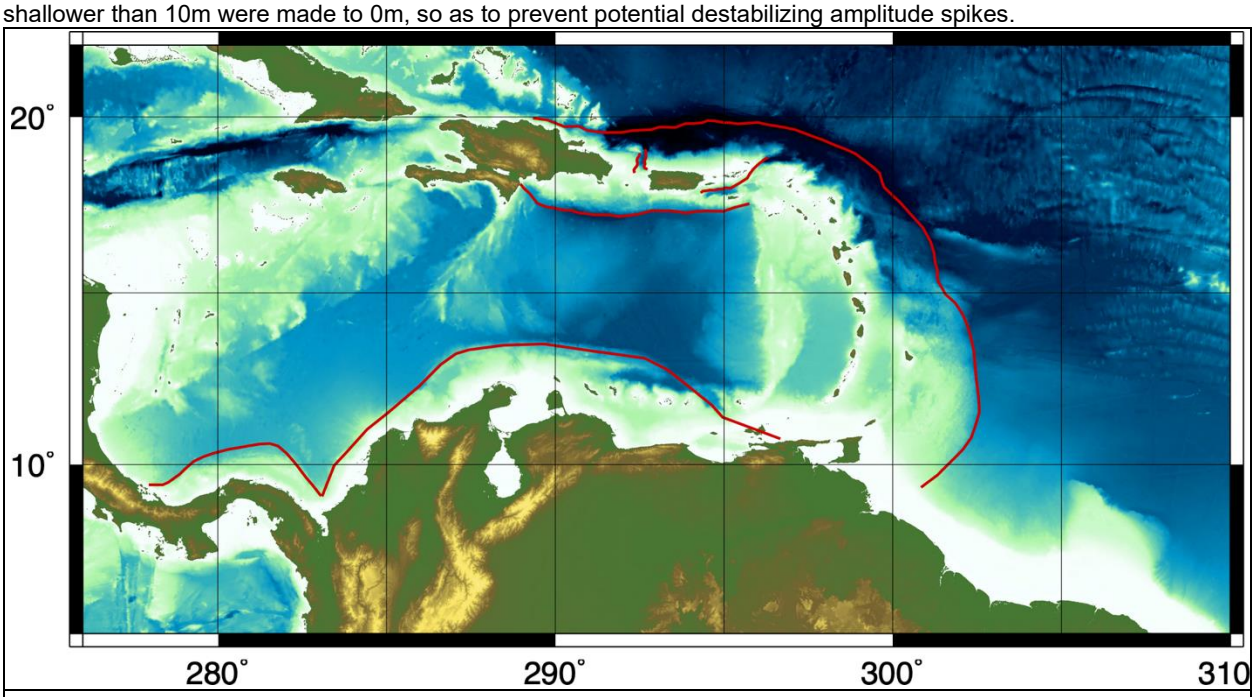

Figure 3-1 Computational domain, showing the digital elevation model from GEBCO. The sources included in this study are indicated with red lineaments.

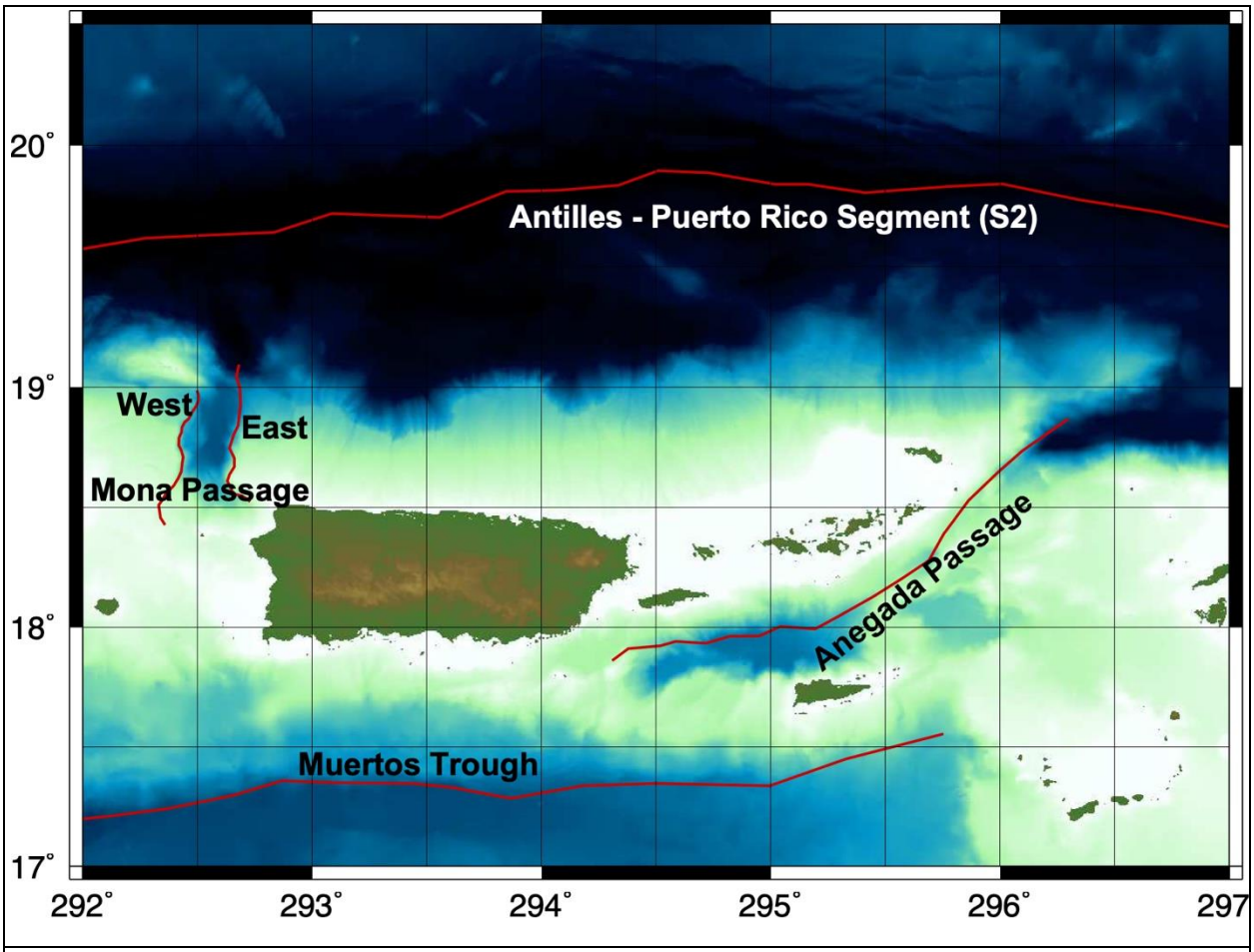

Figure 3-2 Detail of the: computational domain around Puerto Rico and the Virgin Islands showing the digital elevation model from GEBCO. The sources included in this study are named indicated with red lineaments.

4 Tsunami source characterization for PTHA

In this study, we only address tsunami hazard due to earthquake sources. While generally speaking the majority of the tsunami hazard, at least at return periods of general engineering interest, stems from earthquake sources, it is certainly possible that in some cases other sources sch as landslides or volcanoes contribute as well.

The source characterization for the tsunami models consists of a geometrical characterization of the source, recurrence models for earthquakes that define magnitudes and their recurrence rate, and a generation mechanism for slip distribution on the fault.

4.1 Geometrical representation of the fault surface

The subduction zone source representations used in this study are based on the Slab2.0 model of Hayes (2018). We fit the depth contours for every subduction zone with a set of quasi-rectangular subfaults that are small enough to represent the slip variability of large tsunamigenic earthquakes (Figure 4-1). The nominal dimension for these elementary subfaults is 30 km along strike by 10 km in the dip direction but varies according to the curvature of the fault. In order to capture the curvature of the subduction interface, these subfaults are further divided into small patches of 1x1 km. This fine subdivision is strictly meant to accommodate the geometrical complexity; for the actual analysis, the slip on every 30x10 km subfault is uniform.

4.2 Earthquake recurrence model

The earthquake recurrence model defines the magnitude of earthquake with their rate of occurrence. In seismic hazard practice the most common magnitude distributions that are used are the (truncated) Gutenberg-Richter (G-R) relation, the Maximum Magnitude (MM) model and the Characteristic Model (CM). Whereas the G-R model is most often used to describe the background seismicity, it is often assumed that the MM and CM models are more appropriate for large faults. In any case, it is important to define the upper limit for the magnitude that can occur on a fault and for this purpose we make use of earthquake scaling relations. For example, for any rupture configuration we can determine the area (A – km^2), which through the published scaling relations (Figure 2-2, Strasser et al., 2010):

$$M = 4.441 + 0.841 * \log(A), \sigma = 0.286$$

gives us magnitude (M), and thus earthquake moment (M_0 – in Nm):

$$M = \frac{log(M_0) - 9.1}{1.5}$$

The average slip (D) is then obtained through:

$$D = \frac{M}{\mu A}$$

where μ is the elastic shear modulus, we have used a typical crustal value of 30 GPa. In the first equation, the sigma term represents the aleatory variability as the standard deviation of the distribution around the mean. We approximate this distribution using a discrete set of alternative values (-2σ, -σ, median, +σ, +2σ) with weights derived from the normal distribution (.4, .24 and .06 for median, ±σ and ±2σ respectively).

Various authors have developed scaling relationship for subduction zone earthquakes, which vary significantly due to different assumptions and regression models used. In order to take these different views of the earthquake scaling relations into account, we have applied several logic tree branches that represent these different models. The equally

weighted models we considered are from Strasser et al., 2010, Papazachos et al. (2004) and Murotani (2008, 2013) (Figure 2-2).

4.3 Generation of slip models

In previous analyses (e.g. Thio et al., 2010), we have used uniform slip models to produce tsunami waves. At local distances however, the slip variability is an important factor and asperities with large amounts of slip can cause significantly higher tsunami waves, especially locally, as is illustrated by the recent Tohoku earthquake where the maximum slip exceeded the average slip by at least a factor of 2.

Murotani et al. (2008) studied the slip distributions of several subduction zone earthquakes and found a ratio of maximum slip over average slip of 2.2. To include this aleatory slip variability, we used variable slip rupture models with one third of the rupture as an asperity with twice the average slip and the other two-thirds of the rupture at half the average slip. In order to achieve uniform long-term slip, we computed a total of three scenarios for each event where the asperity occupies every part of the rupture once. This way, we avoid the risk that in some areas the hazard is over- or under-estimated due to incomplete or overlapping asperity coverage offshore.

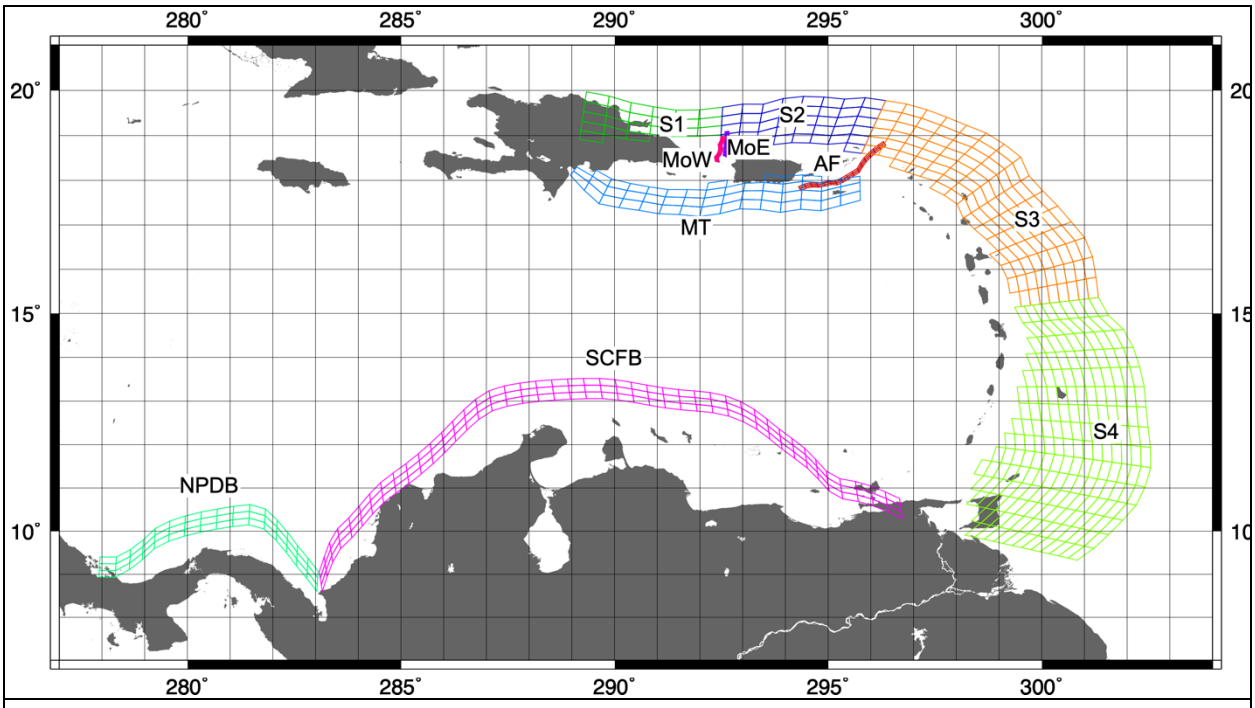

Figure 4-1 Source grids for the contributing sources in this analysis. The Antilles trench sources have been sub-divided into the 4 segments indicated with different colors (S1-S4). MT – Muertos Trough, MoW/MoE – Mona Passage East/West, AF – Anegada Fault, SCFB – South Caribbean Fold Belt, NDDB North Panama Deformed Belt.

5 Earthquake sources

5.1 Introduction

For the development of the earthquake sources it is desirable to follow the USGS NSHM model to ensuer consistency of the earthquake and tsunami hazard models. In some cases, it may be necessary to deviate from that model where local details may have a significant effect on tsunami generation, or where significant disagreements exist that may be important for tsunami generation but not for seismic ground motion models, and there are several sources that are not included in the NSHM due to their distance to the islands (e.g. lesser Antilles trench). In this section, we describe our preliminary model and also present some some alternative models that have been developed for various seismic hazard purposes in the region. We will abridge and refer to the USGS model as it becomes available in the near future. A simple earthquake model has been developed to demonstrate the PTHA for Puerto Rico (and Virgin Islands) and how different parts of the islands are sensitive to different sources.

5.2 Tectonic overview

The tectonics of the PRVI region (NE Caribbean) are governed by the oblique subduction of the North American Plate beneath the Caribbean. The nature of the subduction is highly influenced by the late Neogene collision of the Caribbean Plate with the Bahama Platform. Mutiple neotectonic models exist for the region based upon GNSS, seismicity and geologic data (e.g. Sykes and Mann, Calais, Lopez-Venegas, etc...). Despite differences between the models, the common factor is that the region is characterized by broad deformation near the plate boundary including independent movement of the Gonave, Hispaniola, and PRVI microplates.

5.3 Seismicity

The seismic activity data discussed here spans from 2004-2019 based on the PRSN catalog (PRSN DOI). Here we limit the years to the modern broadband epoch (2004) and prior to the beginning of the 2020 Southwest Puerto Rico Seismic Sequence. Crustal seismic activity post the commencement of the sequence is dominated by the near-off shore faults in SWPR. The discussion of seismicity here is also limited to earthquakes with a minimum magnitude of M2.7, the approximate off-shore catalog completeness. While generally the activity is crustal dominated by the Puerto Rico Trench, activity is also significant in the Mona Passage (northwest of PR) and the Anegada Passage (Southwest of PR).

For the current calculations, background seismicity sources have not been included. All the sources were represented as fault sources, with simple maximum magnitude-type distributions. In further revisions, we may include a Gutenberg-Richter type distributions, based on this catalog analysis, as well, and may also consider distributed earthquake sources if deemed necessary.

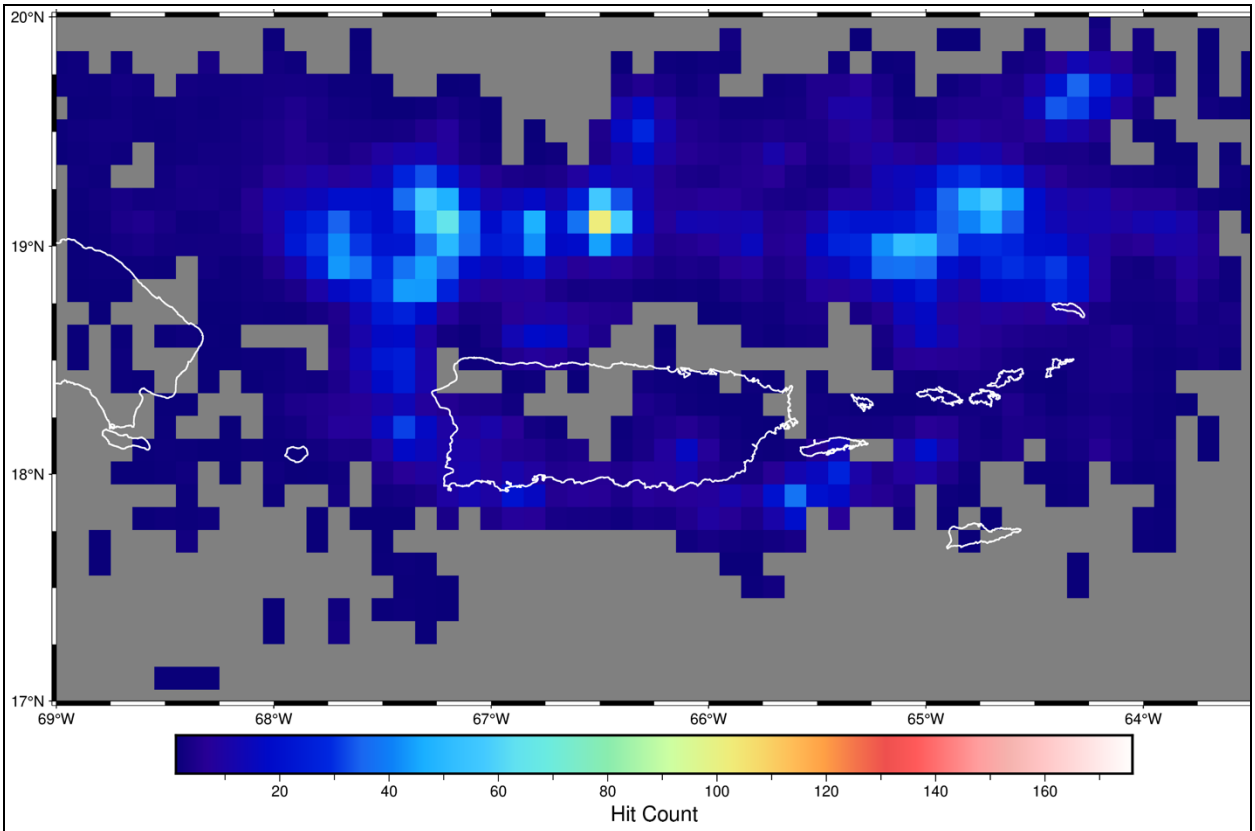

Figure 5-1 Crustal Seismicity 2004-2019 recorded in the PRSN catalog. Here events with a minimum magnitude of 2.7 and depths <25km are included in the heat map. While crustal seismicity is dominated by activity in the Puerto Rico Trench but is also present in the Mona Passage and Anegada Passage.

5.4 Crustal sources

5.4.1 Mona Passage

The Mona Passage is characterized by extensional structures stemming from the rotational motion of the PRVI microplate relative to the Hispaniola Microplate. The region is a known tsunamigenic source zone; the 1918 M7.3 earthquake and tsunami was generated in the Mona Passage. Wave heights of over 6m were recorded in Aguadilla Puerto Rico (Reid and Taber 1919, Doser et al). The exact epicentral location of the 1918 earthquake is debated with some locations on the southern end of the canyon (e.g Doser) whereas other location place the epicentral location on the northern rim (e.g. Aurelio; Reid and Taber). It has been further suggested that the tsunami source may have had a landslide component but a slide with the appropriate age and size has yet to be confirmed. The potential slide suggested by Lopez et al (YEAR) was recently investigated and found to be older than the 1918 earthquake due to an observed patina on the canyon wall (Chaytor et al). With the lack of an identified slide, the purely tectonic tectonic source must still be considered in hazard modeling. Recorded crustal seismicity is consistent with active tectonic processes in the Mona passage region.

5.4.2 Anegada Passage

The Anegada Passage is the result of the differential motion between the PRVI microplate and the Caribbean Plate and demarks the boundary of the PRVI microplate. Recent active source seismic profiling the region has identified structures related to a complex system of strike slip faulting, pull apart basins, and restraining bends (Laurecin et al, 2017) generated by the differential motion. The passage itself is dominated NW-SE extensional motion, particularly within the basins (Laurencin; More Laundry). The 1867 tsunami record wave-heights of ~7-9m in Christenstead, VI

from an earthquake with a magnitude of ~M7.5 (Zahibo et al 2003). Recent modeling of the 1867 earthquake and tsunami suggest that the source was a mixed normal and left-lateral motion either on the northern wall of the Virgin Island Basin or just north of the Basin on the carbonate platform; modeling moreover suggests a source of a lower magnitude of M~7.2 (Barkan and ten Brink, 2010). The former model is consistent with the source suggested by Reid and Taber (1920) and such modeling is consistent with the structures observed in later active source studies (Laurecin et al, 2017) that suggest complex fault interactions in the region. Crustal seismic activity is observed in the region but like Mona Passage at a lower level than the zone directly related to the oblique subduction.

5.5 Subduction and collision zones

For the regional sources, overall geometries and rates are well-established, and for these sources we used the recent plate models of Symithe et al. (2015) and Perez et al. (2018). In this section, we discuss the development of our main parameters are shown in Table 5-1.

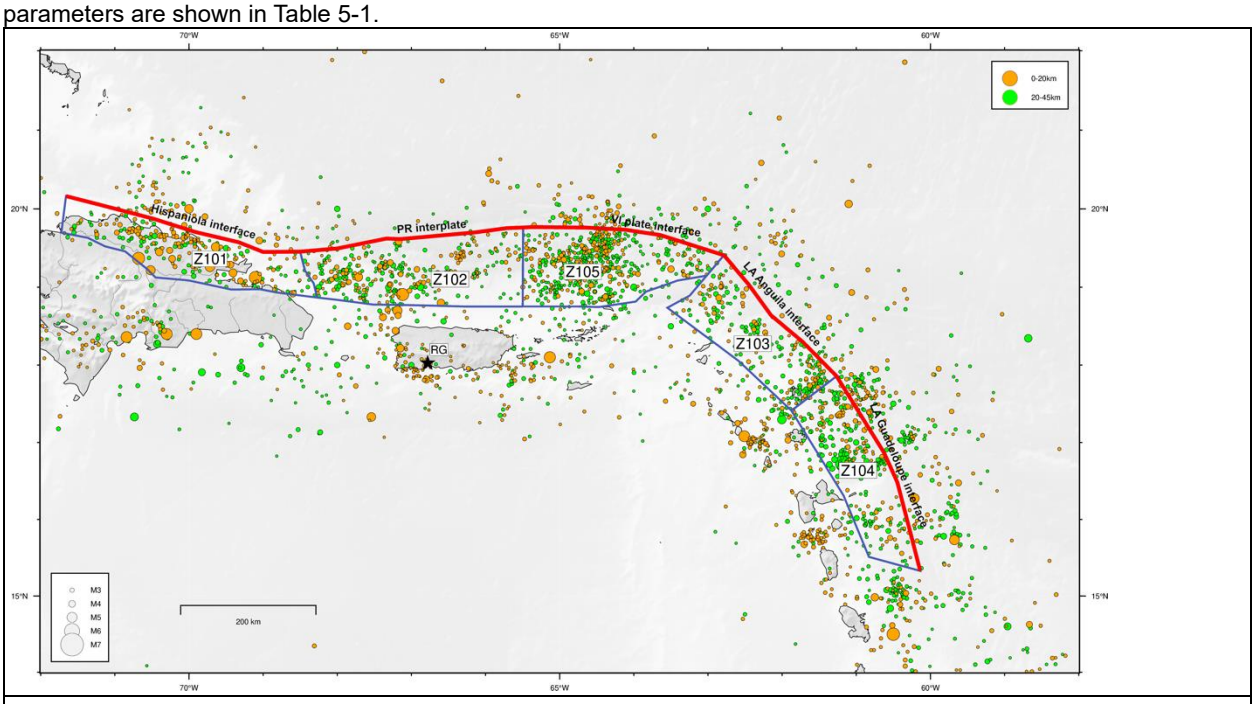

Figure 5-2. The AECOM model of the Puerto Rico trench and northern lesser Antilles trench.

5.5.1 Puerto Rico trench

Regional geophysical, seismological and geodetic studies indicate that the subduction zones in the northeast Caribbean region have complex geometries and characteristics that change along the length of the plate boundary. The geometries of the subduction zones used in the source model are based on previous geological and geophysical studies (e.g., Dolan et al.,1998; Grindlay et al., 2005; ten Brink, 2005; ten Brink et al., 2004, 2009, 2012; Rodríguez-Zurrunero et al., 2020), analysis of our composite seismicity catalogue (Section 3), and geodetic data for the northeast Caribbean region (Jansma et al., 2000; Jansma and Mattioli, 2005; Manaker et al., 2008; ten Brink and Lopez-Venegas, 2012; Calais et al., 2016).

In the 2024 AECOM model, based on the physiographic expression of trenches, changes in down-dip geometry, presence of cross-cutting structures such as the Mona Rift, and the variation in seismic coupling, five primary subduction zone sources were defined: the Hispaniola subduction zone (101) on the west, the Puerto Rico trench and Virgin Islands subduction zone segments (102 and 105).

In the Powell center model, that concentrated on the larger tsunamigenic earthquakes, this subduction zone was divided up into two main segments, the Hispaniola segment and the Puerto Rico – Virgin Island segments as part of the larger Caribbean Arc, which also encompasses the less Antilles subduction zone. In the latter model, the Antilles trench is defined as the arc that separates the Caribbean Plate from the Atlantic Plate along the eastern and northern boundaries. The Antilles trench is subdivided into four segments, with first two segments corresponding to the Puerto

Rico trench, with very low fault normal rates. This subdivision is based on morphology of the subducting crust, changes in geometry, plate boundaries and related changes in convergence rate.

The physical characteristics of these sources are presented in Table B-7. Recent research suggest that the Muertos thrust fault system is not a true subduction zone (Granja Bruna et al., 2010), and so this structure was described in the section on crustal faults.

5.5.2 Lesser Antilles trench

The Lesser Antilles subduction zone trench extends over 1200 km in an N-S direction from approximately 10° N to 19° N (Benz et al, 2011). Subduction of oceanic crust of the South American and North American tectonic plates beneath the Caribbean plate occurs as a result of the eastward migration of the Caribbean plate over the oceanic crust at a rate of about 20 mm/yr (De Mets et al., 2010; Symithe et al., 2015). The suture between the North American and South American plates intersects the Lesser Antilles trench at approximately 15.3°N, where there is a northwest trending bend in the trench (Figure 4-2). Historical accounts of great earthquakes and instrumentally recorded seismicity in the Caribbean region indicate that subduction and underthrusting of the slab is an ongoing process, and that future large magnitude earthquakes are likely to occur on this subduction zone. Large earthquakes attributed to the northern portion of the subduction zone occurred in 1690, 1839, 1843 and 1888 (McCann and Pennington, 1990; Feuillet et al., 2011; Hough, 2013). The majority of historical seismicity has occurred north of 14° N.

The interface between the top of the subducted plate and base of the Caribbean plate dips west between approximately 9° in the south to 15° at the north. The interface is inferred to occur at depths around 40 km to 50 km near Trinidad. The down-going slab steepens beneath the Tobago Basin (between Tobago and Grenada) to the west-northwest and descends at a dip of approximately 45° from a depth of approximately 55-60 km to 200 km.

The deeper portion of the subducted slab (i.e. Wadati-Benioff zone) also increases in dip to approximately 55o on the northern portion of the Lesser Antilles subduction zone.

In the vicinity of Trinidad, the southern margin Lesser Antilles subduction zone terminates against the continental portion of the South American plate. The transition from subduction on the eastern plate boundary to the strike-slip El Pilar fault in northern Venezuela (i.e. southern boundary) occurs beneath, north and east of Trinidad. The configuration of this transition is complicated. Because the South American oceanic crust and continental crust are sutured east of the subduction zone, these two components of the South American plate must decouple as the Caribbean plate migrates eastward. This results in an east-west trending, steeply north dipping slab tear between the oceanic and continental portions of the South American plate (Perez and Aggarwal, 1981; Russo et al., 1993; Clark et al., 2008a, b), which occurs north of the Paria peninsula in Venezuela and Trinidad.

The complicated interaction between the Caribbean and South American plates may affect the Lesser Antilles intraplate maximum earthquake potential near the southern boundary. Analysis of seismicity indicates a higher level of intraplate deformation and seismicity at the southern end of the subduction zone, than to the north. This suggests that a component of the strain energy resulting from the relative motion between the Caribbean and South American plates is released through internal deformation of the two plates. Another important consideration in estimating the maximum magnitude and potential for a great earthquake on the subduction zone interplate is the effective rate of convergence (i.e. seismic coupling) on the subducting slab interface.

For the AECOM model, two Lesser Antilles subduction zone segments on the north east (103 and 104) (Figure 5-2), whereas the Powell Center model has the entire northern part of the lesser Antilles trench as a single segment (Figure 4-1). In this model, the lesser Antilles trench is formed by the eastern segments 3 and 4, which show the largest convergence rates. Around 16 degrees latitude, the Tiburon rise and Barracuda Rise enter the subduction zone, and seismic imaging show significant deformation related to their subduction, including an apparent offset in the trench (Laigle et al., 2013). The boundary between segments 3 and 4 is delineated in this location since it is likely that these features act as an impediment to rupture propagation.

5.5.2.1 General characteristics of the lesser Antilles trench

The readily available literature on the Antilles subduction zone was reviewed to assess whether there is strong evidence for one or more potential segment boundaries in order to develop potential rupture length scenarios that can

then be used to estimate maximum magnitudes (Mmax), rather than assuming a magnitude range or a theoretical maximum assuming the entire Lesser Antilles subduction zone can rupture in a single earthquake.

Subduction zone segments are typically based on one or more of the following characteristics: (1) a significant change in trend, (2) significant change in geodetic displacement direction and/or rate, (3) significant change in historical seismicity rate and/or pattern, (4) a distinct change in the character of the seafloor or a large seamount on the subducting Pacific plate at the trench and/or deformation of the forearc on the upper plate of the subduction zone, (5) geophysical surveys and historical seismicity data that delineate the subsurface plate geometry, and (6) intersection with other major faults or tectonic boundaries. There is some debate about whether some of these types of features have the potential to limit rupture, and there have been exceptions to these in worldwide subduction zone earthquakes; however, there also have not been any historical or known paleoseismic subduction zone earthquakes that have ruptured an entire subduction zone with a length similar to the 1200 km long estimate for the Lesser Antilles subduction zone. Historical subduction zone earthquakes worldwide with a rupture length > 800 km have been partial segments of longer subduction zones (e.g., Alaska 1957, 1964; Chile 1960, 2010; Sumatra 2004).

There are no known studies of paleoseismic evidence of prior earthquakes for the Lesser Antilles subduction zone to include as a basis for segmentation. The available data on the known historical earthquakes on the Lesser Antilles subduction zone (Feuillet et al., 2011; Hough, 2013) indicate that two earthquakes in 1839 and 1843 likely ruptured the northern segment of the subduction zone from approximately 15° N to the north end of the segment near Barbuda. Based on these events, the difference in instrumentally recorded historical seismicity north and south of approximately 15o N, and the change in trend of the trench, dip of the subducting slab and width of the forearc to the north of 15° N (Figure 4-2), we have inferred that the most likely future interplate subduction zone rupture would occur on the southern segment between about 10° N and 15° N. The rupture length of this segment is approximately 500 km. As shown on Figure 4-2, the likely seismogenic width decreases from south to north as the dip on the interface increases. The width of the likely rupture area was delineated based on the cross- sections of seismicity on Figure 4-2, from Benz et la. (2011) and Symithe et al. (2015), and the heat flow modeling results of Gutscher et al. (2013) (Figure 4-2). An average width of 233 km was calculated from the 500 km length of and area within the rupture scenario polygon.

5.5.2.2 Maximum Magnitude

Previously published estimates of the maximum magnitude (Mmax) for the Lesser Antilles subduction zone are primarily based on extrapolation of historical seismicity and/or theoretical estimates (e.g. McCaffrey 2008; Rong et al., 2014). McCaffrey (2008) assumed that all subduction zones, including the Lesser Antilles, are capable of generating a Mw 9.0-9.5 earthquakes based on conservative assumptions including full (100%) coupling and the full fault length rupture. For the complete ~1200 km Lesser Antilles rupture the estimated maximum earthquake is Mw 9.3 with an approximately 1600-year recurrence for a Mw 9.0 earthquake. Rong et al. (2014) calculated a maximum magnitude of Mw 9.0 for all subduction zones bounding the Caribbean Plate (including Lesser Antilles) based on extrapolation of the historical seismicity and estimated maximum probable earthquakes of Mw 8.7 to 8.8 for a 500-year to 1000-year return period. Berryman et al. (2013) provide a best estimate of Mw 8.7, with a range of Mw 8.0 to 9.4.

Schellart and Rawlinson (2013) evaluated multiple parameters for subduction zones worldwide and ranked (with a score (S) of 1 to 6) 200 km-long trench segments within each subduction zone in terms of their predicted capability of generating a subduction zone interplate earthquake with Mw > 8.5. Based on their analysis, the Lesser Antilles-Puerto Rico subduction zone segments had high scores (average S = 5.1, range = 4–6). The two southernmost segments were scored 4 and 5.

The Lesser Antilles subduction zone has had no large (M~7.5) instrumentally recorded earthquakes. Two earthquakes, in 1839 east of Martinique and 1843 from east of Dominica to Barbuda at the north end, likely occurred on the subduction zone. The 1839 earthquake had an estimated magnitude of Mw 8.0 (Feuillet et al., 2011). The magnitude of the 1843 earthquake has been variable estimated at 7.5 to 8.0 (Bernard and Lambert, 1988; ten Brink et al., 2011), 8.3 (U.S. NGDC as reported by Hough, 2013), 8.0 to 8.5 (McCann et al., 1982), 8.5 (Feuillet et al., 2011), or greater than 8.5 (Hough, 2013). Because of its magnitude and location at a subduction plate boundary, this earthquake, which did not cause a tsunami, is most often interpreted as a thrust event on the plate interface (Hough, 2013).

Using the empirical equations outlined in Section 4.0, the estimated length and rupture area for the southern segment was used to estimate interplate Mmax values ranging from Mw 8.6 to Mw 8.8. Four magnitude values were estimated

based on the estimated magnitudes reported above with a weight assigned to each value. The middle of the three Mmax values estimated based on length/area is weighted the most (8.7, 0.5), with the lower (8.3, 0.1 and 8.5 0.3) and higher (8.9, 0.1) values weighted according to our judgement as to how less likely that the Mmax is less or greater than the middle value.

5.5.2.3 Interplate Coupling

The degree of coupling on a subduction zone is used to assess the amount of the plate convergence rate that is a result of rupture during great earthquakes on the interplate versus the amount of plate movement that occurs aseismically. Worldwide data compiled and analyzed by Heuret et al. (2011) indicate the average seismic coupling coefficient worldwide is generally found to be low (c = 0.25 ± 0.30) and calculate that the overall coupling coefficient on the Lesser Antilles subduction zone is 0.08 with the trench normal component coupling coefficient of 0.13. Berryman et al (2013) indicate a preferred coupling coefficient of 0.5 with a min-max range of 0.3-0.7. Sholz and Campos (1995, 2012) do not include the Lesser Antilles in their evaluation of subduction zone coupling worldwide.

Symithe et al. (2015) conclude that the GPS data from around the Caribbean plate are consistent with a Lesser Antilles arc that moves coherently with the rest of the Caribbean plate. The GPS data are not consistent with the 5 mm/yr motion of a northern Lesser Antilles rigid sliver proposed by Lopez et al. (2006) and also exclude the slip partitioning model proposed by Feuillet et al. (2010) with 5 to 10 mm/yr of distributed deformation throughout the northern Lesser Antilles. Therefore, Symithe et al. (2015) state that the observed active faults within the arc and forearc must therefore be accumulating strain at a rate of at most 1–2 mm/yr, the average residual of the best fit model in the Lesser Antilles. This indicates there is approximately 18 mm/yr of plate convergence that may be accommodated by seismic displacement on the subduction zone interface. Symithe et al. (2015) modeled the geodetic deformation throughout the Caribbean and across the Lesser Antilles arc and concluded that the best fit model indicates that there is very low, plate normal coupling along the Lesser Antilles subduction zone ranging from 1.2-2.2 mm/yr on the northern segment and 2.3 - 3.1 mm/yr on the south. These rates equate to a coupling coefficient of 0.06 to 0.15, which is similar to the range estimated by Heuret et al. (2011).

Based on the recent modeling by Symithe et al. (2015) and other prior researchers noted above that interpret a low coupling coefficient for the Lesser Antilles, slip rates (in mm/yr) for the southern segment of 2.3 (0.3) and 3.1 (0.5) are considered the most representative and 4.0 (0.2) was included as an upper bound (i.e. 20% or 0.2 coupling coefficient).

5.5.3 Muertos trough

For the Muertos trough we defined two segments, which have very different convergence rates due to local plate complexities. Although it is a relatively short subduction zone, it is thought to be capable of significant earthquakes (ten Brink et al., 2011). It is intersected by the boundary between the Hispaniola and Puerto Rico-Virgin Islands microplates, which results in a significant change in convergence rate from 4.5 mm/yr along the western segment to 1.3 mm/yr along the eastern segment (Symithe et al., 2015). We allow for full rupture with a weight of 25%, but the rate in that case is defined by the lowest of the two, 1.3 mm/yr.

5.5.4 South Caribbean Deformed Belt

The South Caribbean Deformed Belt is a wide accretionary margin-type structure separating the South America plate from the Caribbean plate. Lizerazo et al. (2021) found strong evidence of seismic coupling along this boundary, and GNSS data for this region shows complex and significant differential motions across the entire northwestern part of South America (Mora-Paez et al., 2021) We modeled this belt with a main thrust fault along it northern border, with a strong arc-like shape and significant variation in convergence rate from west to east. We identified three segments, a SW-NE trending western segment, an EW trending central segment and a NW-SE trending eastern segment with convergence ranging from 6 mm/yr in the west to 1 mm/yr in the east (Symithe et al., 2015).

5.5.5 North Panama Deformed Belt

The north panama Deformed Belt (NPDB) is part of a larger zone of convergence on the Caribbean side of the Central America Isthmus. Although seismicity is low, there is evidence for large (M7-8) earthquakes that have occurred in the last few centuries (Camacho et al., 1993). On the far western end just across the border with Costa

Rica, a large (Mw=7.7) earthquake occurred in 1991 (Protti and Schwartz, 1994). Estimates for the overall convergence rate in this area range from 6 mm/yr to 11 mm/yr (e.g. Symithe et al., 2017; Perez et al., 2018; Rockwell et al., 2010).

Table 5-1 Main fault parameters.

	Segment	Weight	Rate (mm/yr)	Mmax
Antilles trench	S1	1	2.5	8.9
	S2	1	14	8.4
	S3	1	19	8.3
	S4	1	20	8.8
Muertos	W	.75	4.5	7.5
	E		1.3	7.5
	All	.25	1.3	7.8
Anagada		1	1.5	
Mona East		1	1.5	7.0
Mona West		1	1.5	7.0
South Caribbean Fold Belt	E	.75	1	8.2
	C		4	8.1
	W		6	8.1
	All	.25	1	8.6
North Panama Deformed Belt	W	.75	11	7.4
	E		6	7.8
	All	.25	6	8.2

6 Results

6.1 Offshore hazard

Based on the aforementioned earthquake recurrence parameters and using the methodology explained in section 2 we performed a preliminary probabilistic offshore tsunami hazard analysis with the results shown in Figure 6-1. Here, the hight of the bars indicates the offshore exceedance amplitude for a return period of 2475 years (the ASCE 7-22 standard) for 29 points on the 100m contour around Puerto Rico and the Virgin Islands. The highest hazard is found along the northern coast of Puerto Rico and the eastern end of the Virgin Islands. These are locations that have direct exposure to some of the largest and active sources, and is therefore not too surprising. Along the southern shores, the hazard tends to be significantly lower

These results show the exceedance amplitudes for 2475 years to be on the order of 2 to 5 meters, but given the simplicity of this model we expect the final results may differ significantly in some or all localities. In Figure 6-2 we show and example of the hazard curve at one example point (the others are shown in Appendix B) in the Mona Passage as well as the source disaggregation for this point off the southwest of Puerto Rico. The significant sources contributing to the 2475 yr hazard for this point are widely distributed. The biggest contributions come from the Puerto Rico Trench, the northern lesser Antilles trench and the Muertos Trough, but note that the South Caribbean Fold Belt also contributes to the hazard. Compare this to the hazard on the other end of the domain, north of the Virgin Islands (Figure 6-3) where the hazard is much higher, and dominated by the Antilles Trench.

These preliminary results indicate that the probabilistic hazard in general is not dominated by a single source, even for individual points, and it is therefore very important to consider even the more distant sources, especially along the South Caribbean Deformed Belt, with care. The overall patterns seen in these results are not particularly surprising, but give a quantitative estimate of the hazard for different probability levels.

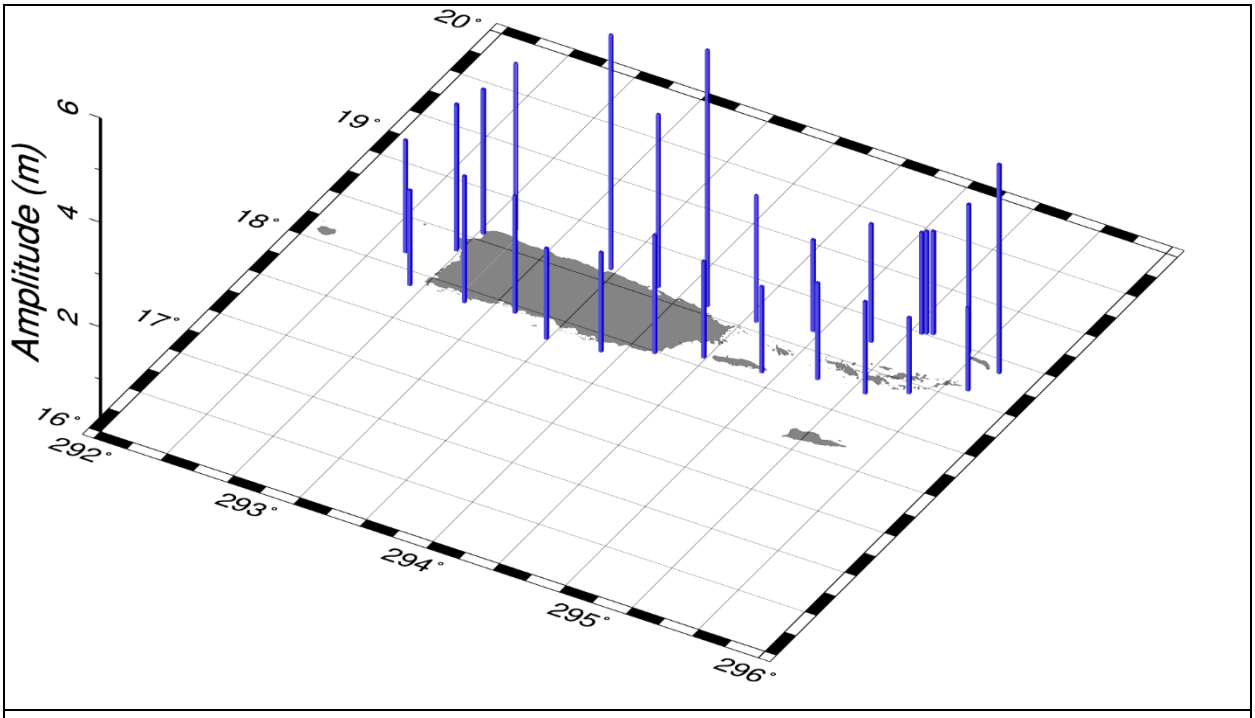

Figure 6-1 Offshore hazard around Puerto Rico and the Virgin Islands showing the 2475 yr hazard.

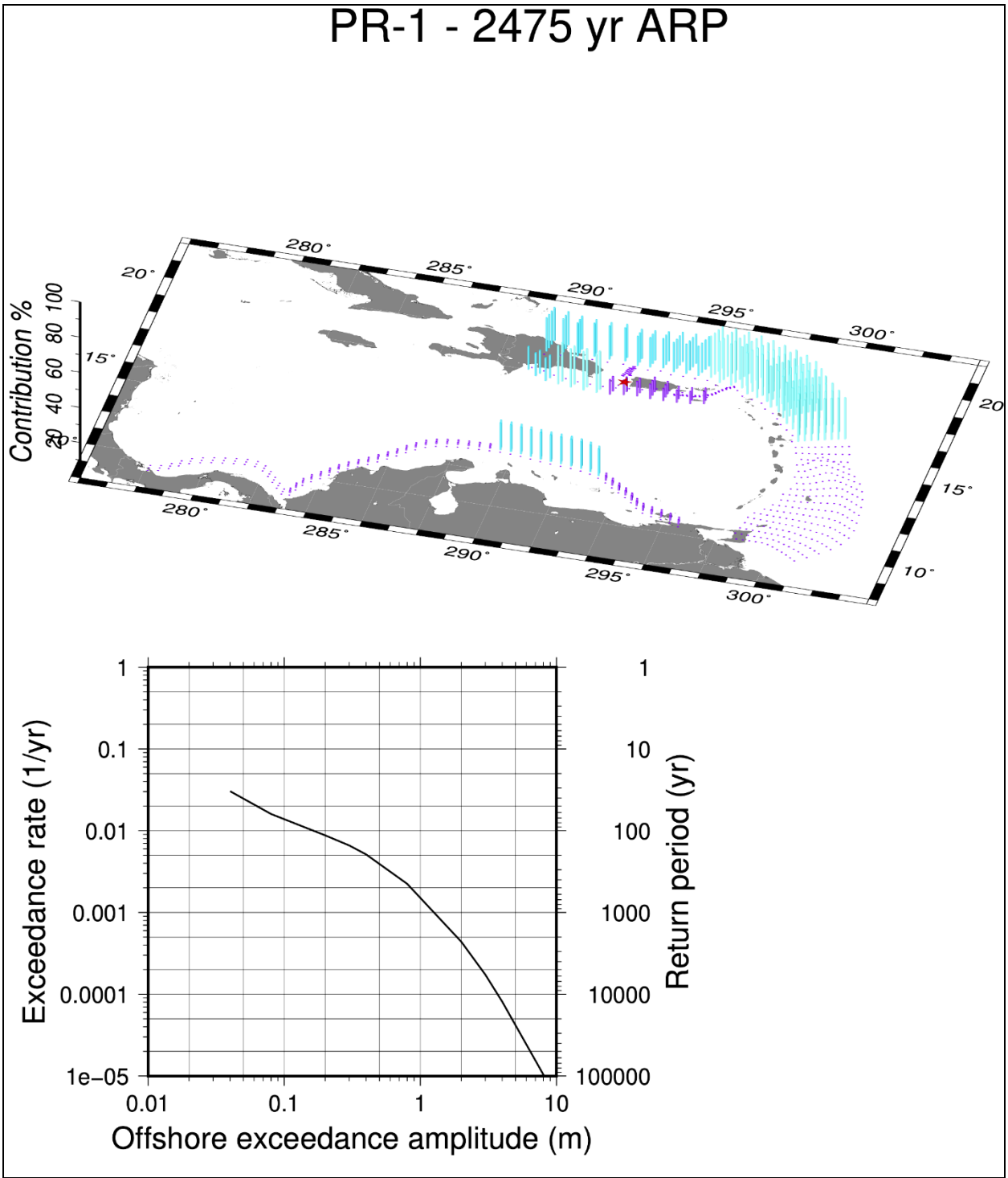

Figure 6-2 Source disaggregation for the 2475 yr hazard in the Mona Passage. The height of the bars indicates the relative contribution to the hazard at the site for this return period. THe complete disaggregation and hazard curves are given in Appendix B.

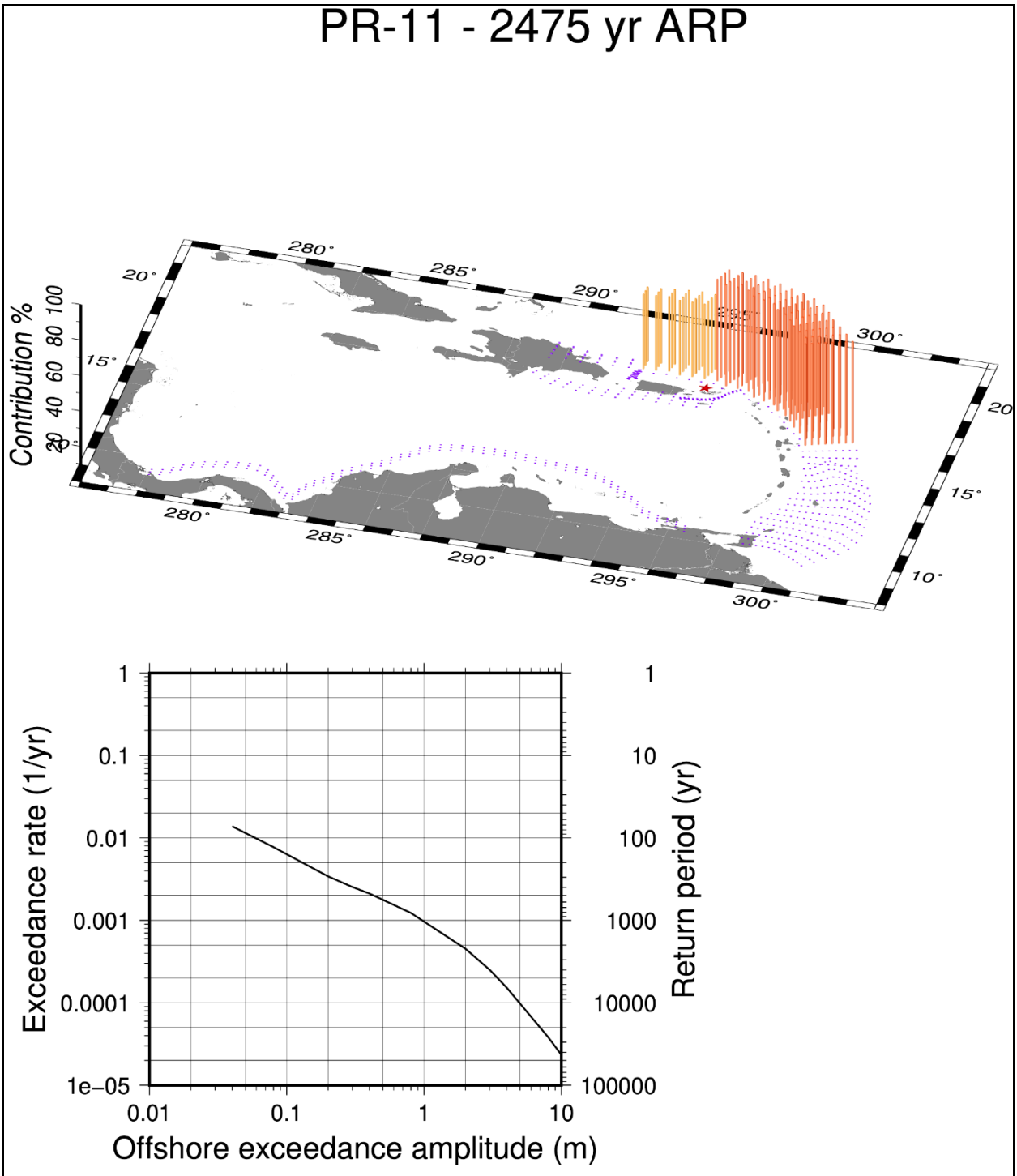

Figure 6-3 Source disaggregation for the 2475 yr hazard north of the Virgin Islands. The height of the bars indicates the relative contribution to the hazard at the site for this return period.

7 Future work

The current hazard results and source characterization should be regarded as preliminary, as the full source model is still awaiting the final USGS model for the National Seismic Hazard Mapping project. Once this becomes available, it will be implemented along the current model and the hazard calculations will be re-run. We will also compute the result for a denser set of offshore points as is presented here, to provide input for further hazard work, such as the ASCE 7-28/34 tsunami design zones.

8 References

ASCE (American Society of Civil Engineers), 2022. ASCE 7-22 Minimum Design Loads For Buildings and Other Structures, Reston, VA.

Bruña, J., Brink, ten, U.S. and Carbó-Gorosabel, A., 2009. Morphotectonics of the central Muertos thrust belt and Muertos Trough (northeastern Caribbean): *Marine Geology*, **263**, p. 7–33, doi: 10.1016/j.margeo.2009.03.010.

Hayes, G., 2018, Slab2 - A Comprehensive Subduction Zone Geometry Model: U.S. Geological Survey data release, https://doi.org/10.5066/F7PV6JNV.

Liu, P.L.F., Cho, Y.S., Briggs, M.J., Kânoğlu, U., and Synolakis, C.E., 1995. Runup of solitary waves on a circular island. *Journal of Fluid Mechanics* **302**, 259–286.

Lizarazo, S. C., Sagiya, T., & Mora-Páez, H. (2021). Interplate coupling along the Caribbean coast of Colombia and its implications for seismic/tsunami hazards. *Journal of South American Earth Sciences*, *110*, 103332. http://doi.org/10.1016/j.jsames.2021.103332

McGuire, R.K., 2004. Seismic hazard and risk analysis, Earthquake Engineering Research Institute, MNO-10, 240 pp.

Mora-Páez, H., Kellogg, J. N., & Freymueller, J. T. (n.d.). Contributions of space geodesy for geodynamic studies in Colombia: 1988 to 2017. http://doi.org/10.32685/pub.esp.38.2019.14

Murotani, S., Miyake, H., and Koketsu, K., 2008. Scaling of characterized slip models for plate-boundary earthquakes. *Earth, Planets and Space* **60**(9), 987.

Murotani, S., Satake, K. & Fujii, Y. 2013. Scaling relations of seismic moment, rupture area, average slip, and asperity size for M~9 subduction-zone earthquakes. *Geophysical Research Letters* **40**(19), 5070–5074.

Okada, Y., 1992. Internal deformation due to shear and tensile faults in a half-space. *Bulletin of the Seismological Society of America* **82**(2), 1018–1040.

Pérez, O.J., Wesnousky, S.G., La Rosa, De, R., Márquez, J., Uzcátegui, R., Quintero, C., Liberal, L., Mora-Páez, H. and Szeliga, W., 2018. On the interaction of the North Andes plate with the Caribbean and South American plates in northwestern South America from GPS geodesy and seismic data: *Geophysical Journal International*, **214**, p. 1986–2001, doi: 10.1093/gji/ggy230.

Rodríguez, I., Bulnes, M., Poblet, J., Masini, M., & Flinch, J. (2021). Structural style and evolution of the offshore portion of the Sinu Fold Belt (South Caribbean Deformed Belt) and adjacent part of the Colombian Basin. *Marine and Petroleum Geology*, *125*, 104862. http://doi.org/10.1016/j.marpetgeo.2020.104862

Savage, J.C., 1987. Effect of crustal layering upon dislocation modeling. *Journal of Geophysical Research: Solid Earth* **92**(B10), 10595–10600.

Savage, J.C., 1998. Displacement field for an edge dislocation in a layered half-space. *Journal of Geophysical Research: Solid Earth* **103**(B2), 2439–2446.

Strasser, F.O., Arango, M.C., and Bommer, J.J., 2010. Scaling of the Source Dimensions of Interface and Intraslab Subduction-zone Earthquakes with Moment Magnitude, *Seismol. Res. Lett.*, *81*(6), 941–950, doi:10.1785/gssrl.81.6.941.

Symithe, S., Calais, E. and Chabalier, J.B., 2015. Current block motions and strain accumulation on active faults in the Caribbean: *Journal of Geophysical Research: Solid Earth*, **120**, p. 3748–3774, doi: 10.1002/2014JB011779.

Uri S ten Brink, W.H.B.C.H.F., 2011. Historical perspective on seismic hazard to Hispaniola and the northeast Caribbean region:, p. 1–15, doi: 10.1029/2011JB008497.

Thio, H.K., Somerville, P.G., and Polet, J., 2010. Probabilistic tsunami hazard in California: *Pacific Earthquake Engineering Research Center Report*, v. **108**, p. 331.

Thio, H.K., Wei, Y., Chock, G., and Li, W., 2017. Development of Offshore Probabilistic Tsunami Exceedance Amplitudes for ASCE 7-16. In Proceedings of the Sixteenth World Conference on Earthquake Engineering, Santiago.

Wald, D.J., and Graves, R.W., 2001. Resolution analysis of finite fault source inversion using one- and three-dimensional Green's functions: 2. Combining seismic and geodetic data. *Journal of Geophysical Research: Solid Earth* **106**(B5), 8767–8788.

Wang, R., Martin, F.L., and Roth, F., 2003. Computation of deformation induced by earthquakes in a multi-layered elastic crust--FORTRAN programs EDGRN/EDCMP, *Computers & Geosciences*, *29*(2), 195–207.

Appendix A Input parameters

The current implementation of the AECOM PTHA (ACM-PTHA) code uses a simple set of input parameters to generate a collection of scenarios that are used to compute the offshore hazard. In this section we present examples of these files. Further documentation will be provided on-line.

A.1 Fault geometry and gridding

Muertos Trough

cont2grid-v1.5	**Remarks**
I_cont-Muertos	Input file name
Muertos-all.xyz	Contour file
90	Convergence azimuth
50 25	Grid LxW (km)
50	Bottom of seismogenic zone
-999	Initial dip

The resulting fault grid is represented in an ASCII file

i_invall-Muertos
295.5213 17.6029 3.77 -99.6 17.5 90.0 100.00 50.07 24.39 0 0 1
295.5195 17.8089 13.41 -93.7 28.5 96.7 100.00 48.47 24.72 0 1 1
295.5179 17.9840 28.46 -92.2 47.2 100.8 100.00 47.39 24.87 0 2 1
295.0632 17.4887 2.62 -99.8 12.0 90.0 100.00 49.91 24.22 1 0 1
295.0669 17.7038 9.66 -94.8 21.1 95.3 100.00 48.69 24.49 1 1 1
.
.
.
.
289.5164 17.7230 3.48 -61.8 16.0 90.0 100.00 47.07 25.18 13 0 1
289.6166 17.8992 13.33 -74.9 32.6 74.5 100.00 42.89 27.32 13 1 1
289.7059 18.0563 27.80 -84.2 42.6 60.6 100.00 40.14 28.82 13 2 1
289.1750 18.0139 7.88 -55.5 41.0 90.0 100.00 48.10 25.40 14 0 1
289.2602 18.1397 25.49 -69.1 52.8 68.3 100.00 44.77 26.08 14 1 1

A.2 Earthquake recurrence model

GetRupMod-v2.5	Remarks
i_GetRupMod	
v2.3	
Muertos	
Muertos	
1	Number of top of ruptures
0.0	Top of ruptures
1.0	Weights of top of ruptures
1	Number of seismogenic depth terminations
35.0	Seismogenic depth
1.0	Weights of the seismogenic depths
7	Number of segmentation models
0 5 9 13 0 9 0	Start of segments
4 8 12 17 8 17 17	End of segments
.7 .7 .7 .7 .2 .2 .1	Weights of segments
1.3 1.3 4.5 4.5 1.3 4.5 1.3	Rate
1. 1. 1. 1. 1. 1. 1.	Coupling
32.e9	Mu = 320 kbar = 32 GPa - 1 bar = 1e5 Pa -> kbar = 1e8 PA = 0.1 GPa
3 2.0	Asperity step, DmaxDav

A.3 Green's functions

For this study we used reciprocal Green's functions. These are computed for a unit (1 m) uplift of the sea surface at the offshore target point. For the current analysis, these have been computed with the in-house code at AECOM, for a linear propagation model on a 30 arcsec grid. The grid has been truncated at the shoreline at a depth of 10m to prevent excessive amplitudes that can destabilize the computations. These Green's functions are stored in multiplexed format, but routines are provided that will demultiplex them.

Appendix B Disaggregation and Hazard curves

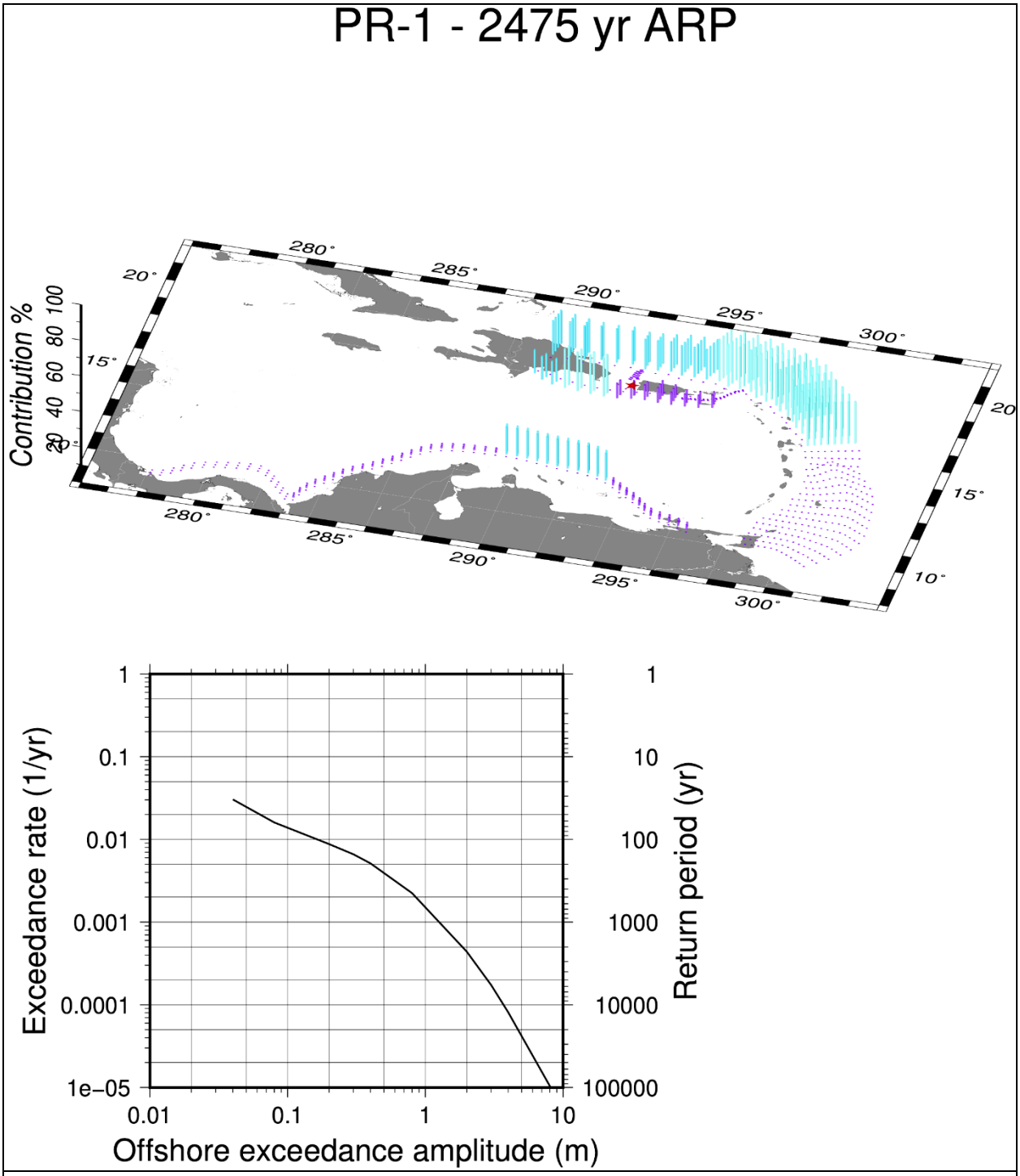

Figure B-1. Disaggregation map and hazard curve for point PR-1

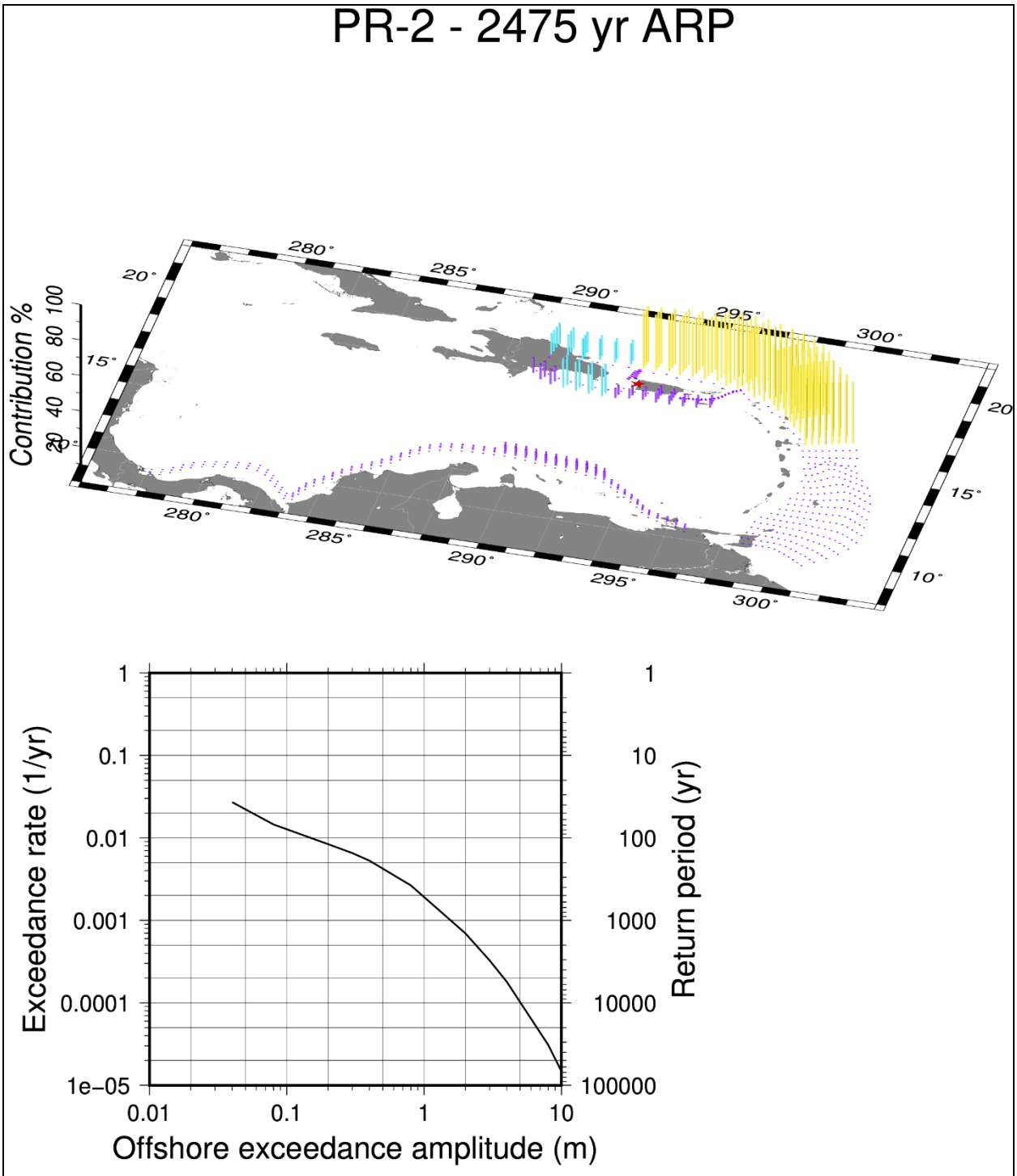

Figure B-2. Disaggregation map and hazard curve for point PR-2

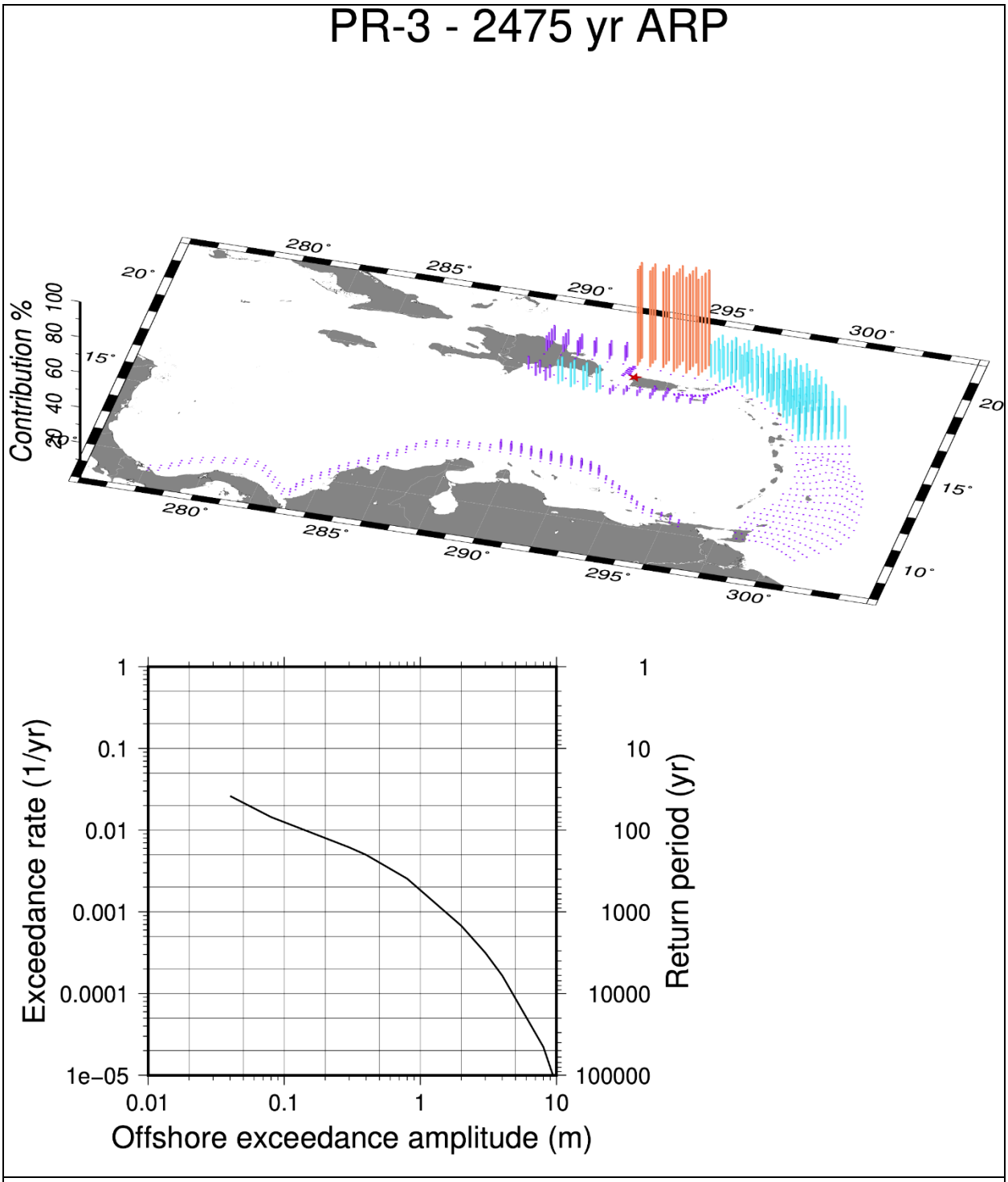

Figure B-3. Disaggregation map and hazard curve for point PR-3

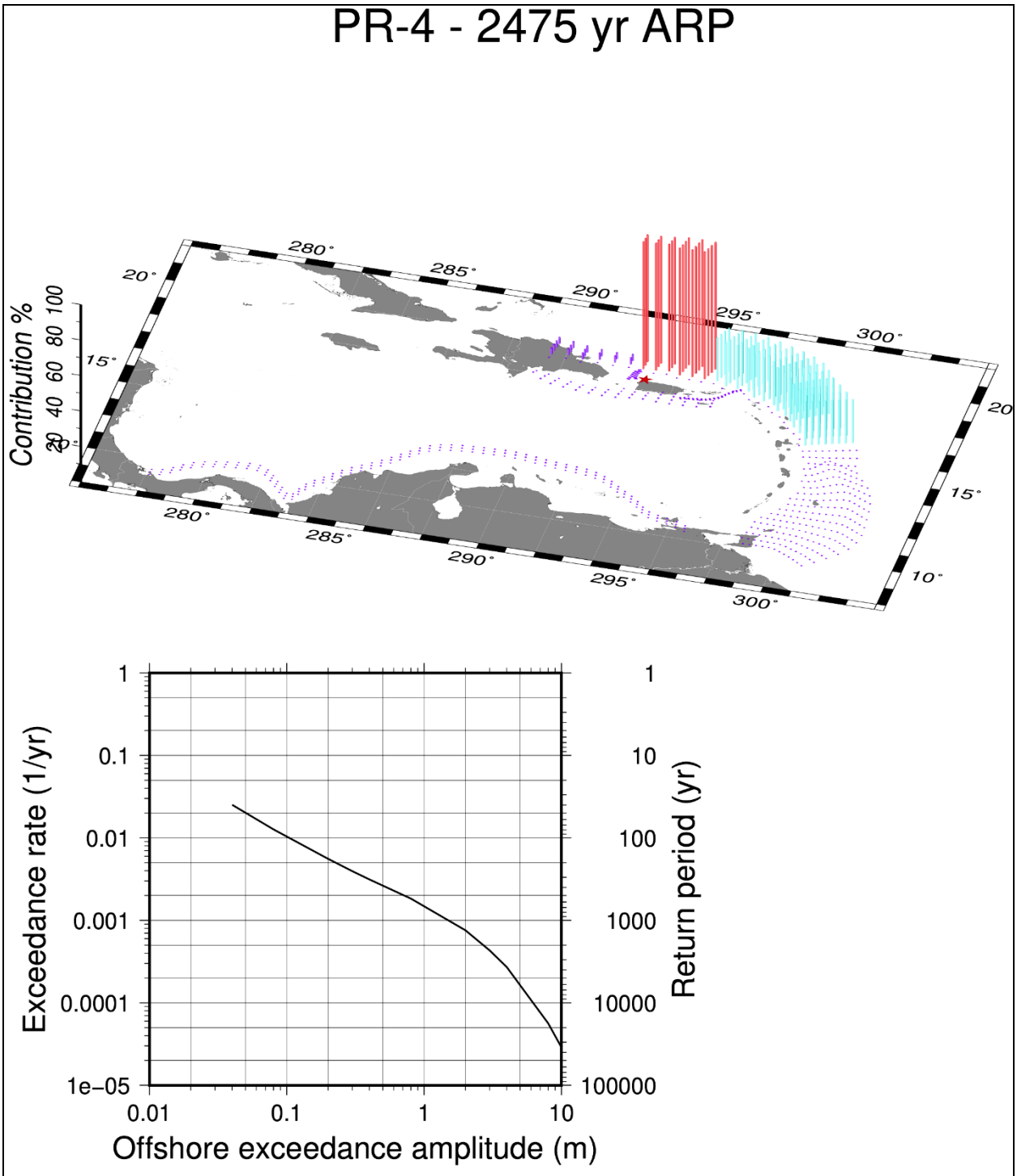

Figure B-4. Disaggregation map and hazard curve for point PR-4

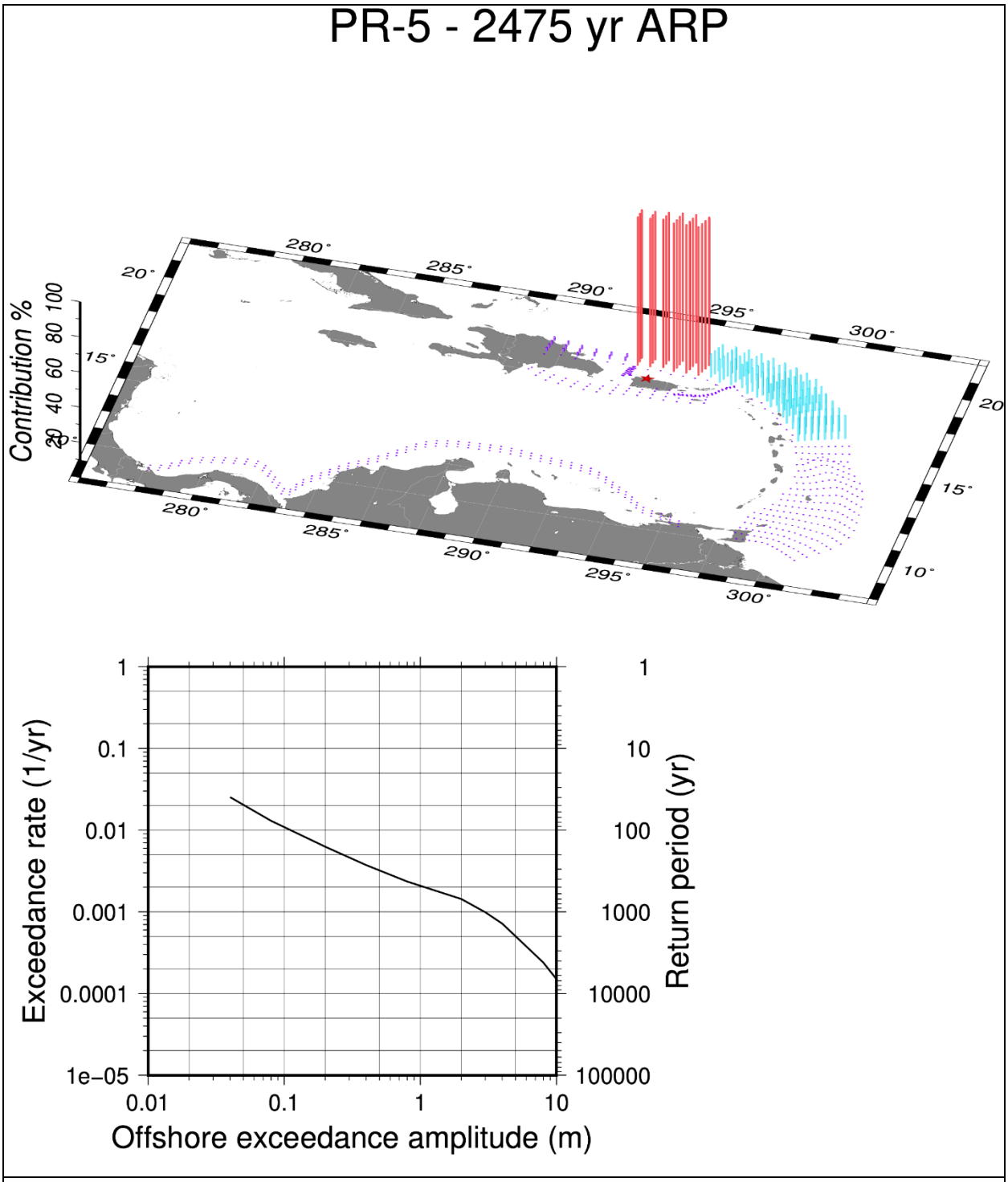

Figure B-5. Disaggregation map and hazard curve for point PR-5

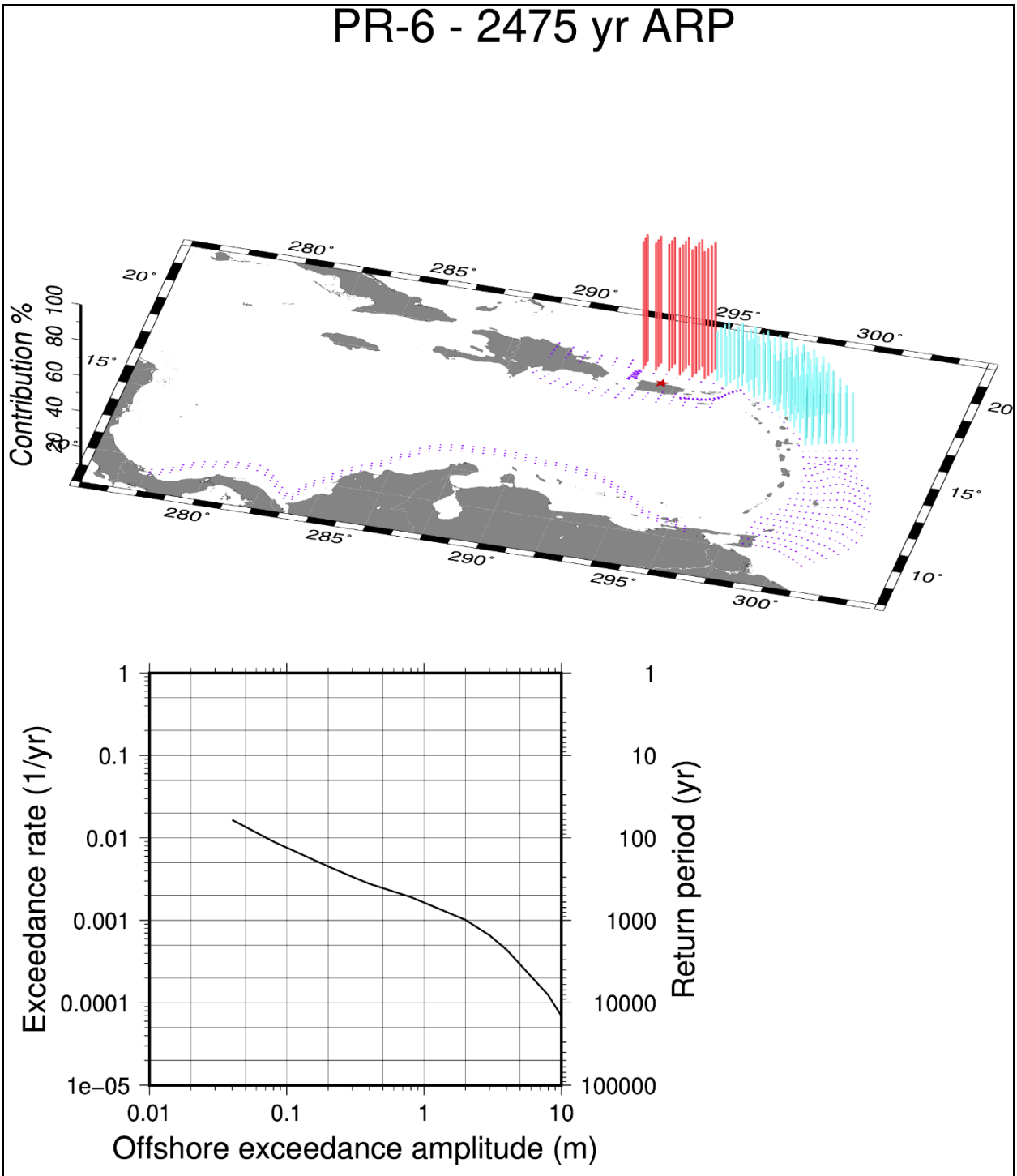

Figure B-6. Disaggregation map and hazard curve for point PR-6

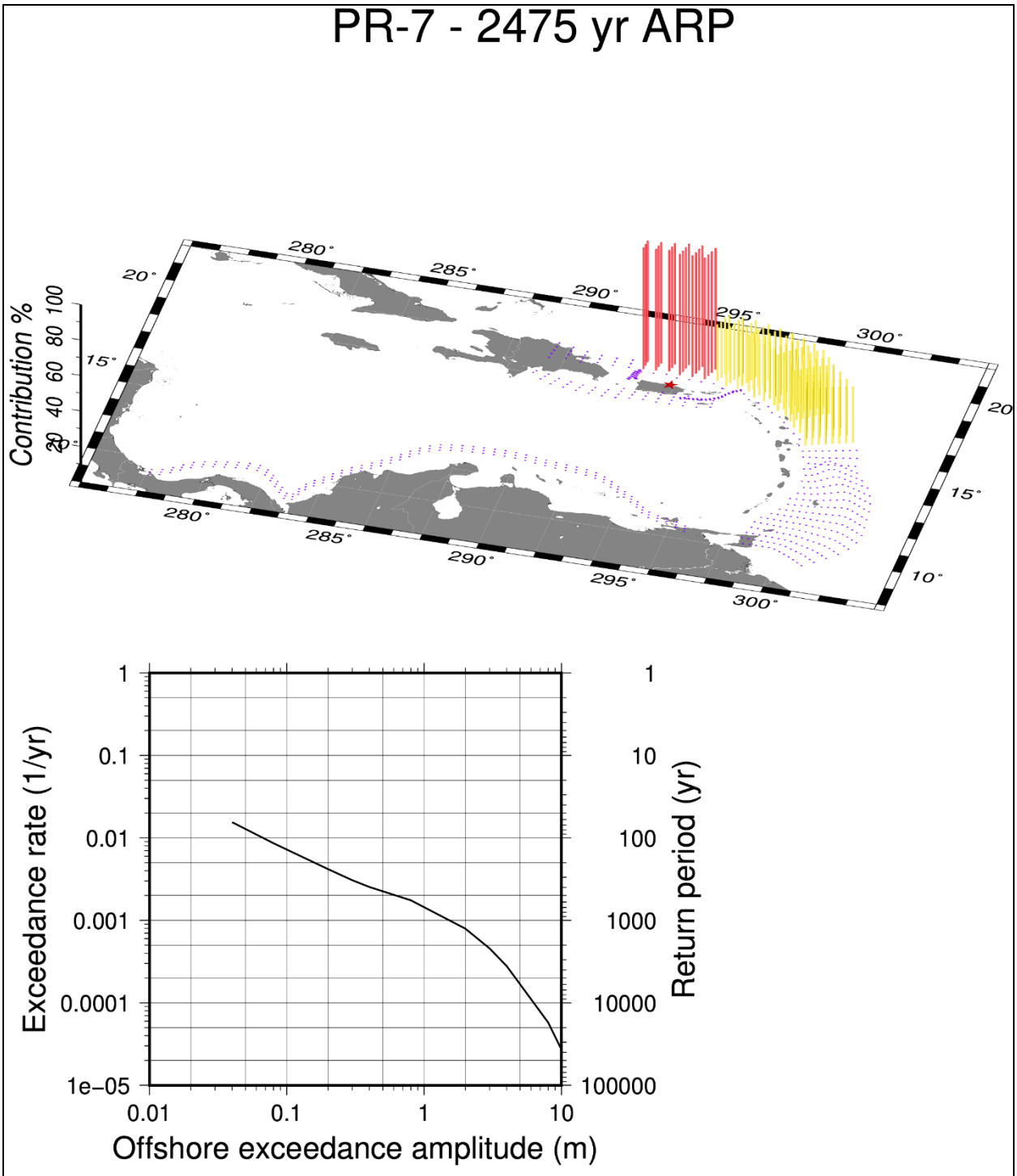

Figure B-7. Disaggregation map and hazard curve for point PR-7

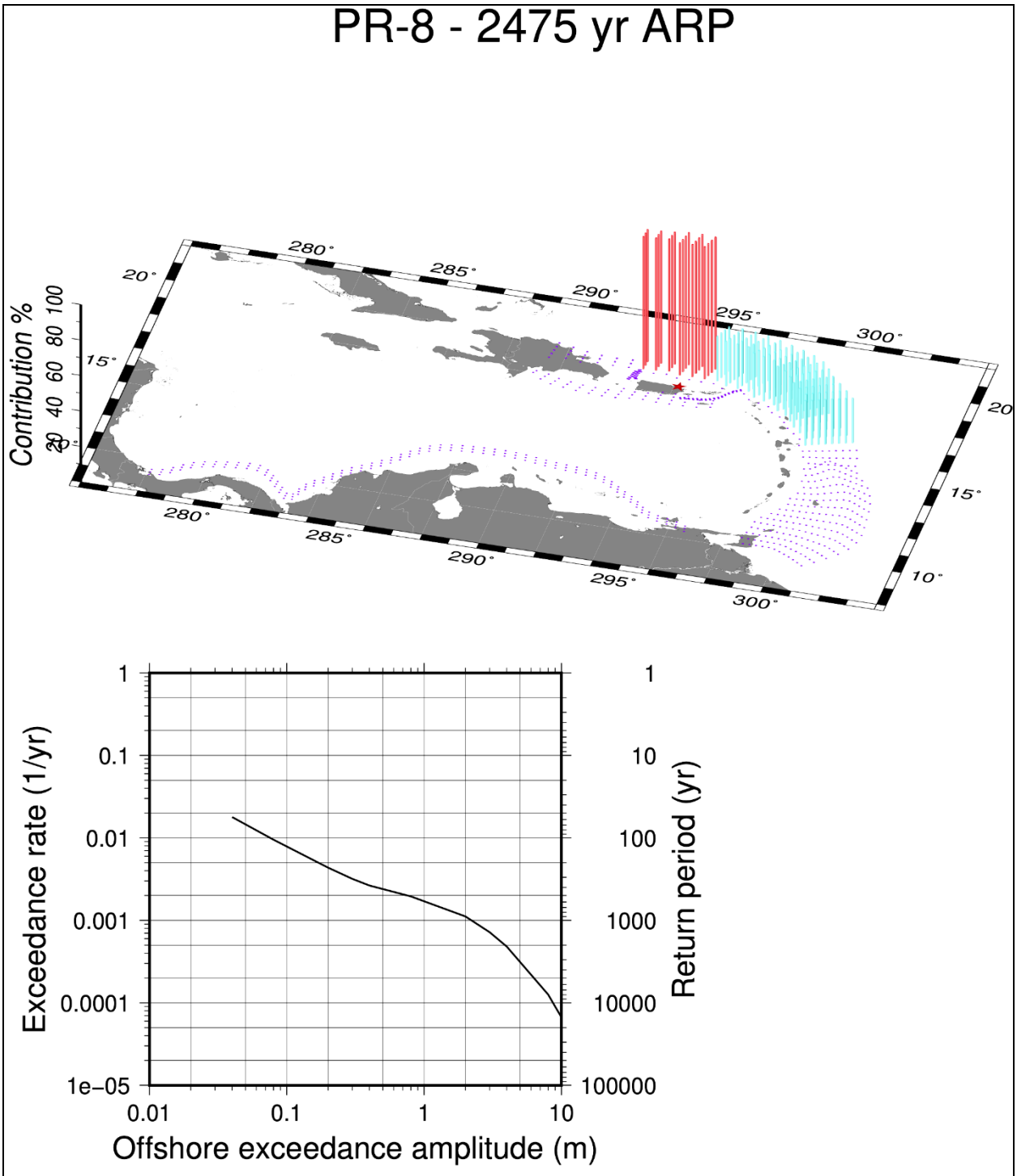

Figure B-8. Disaggregation map and hazard curve for point PR-8

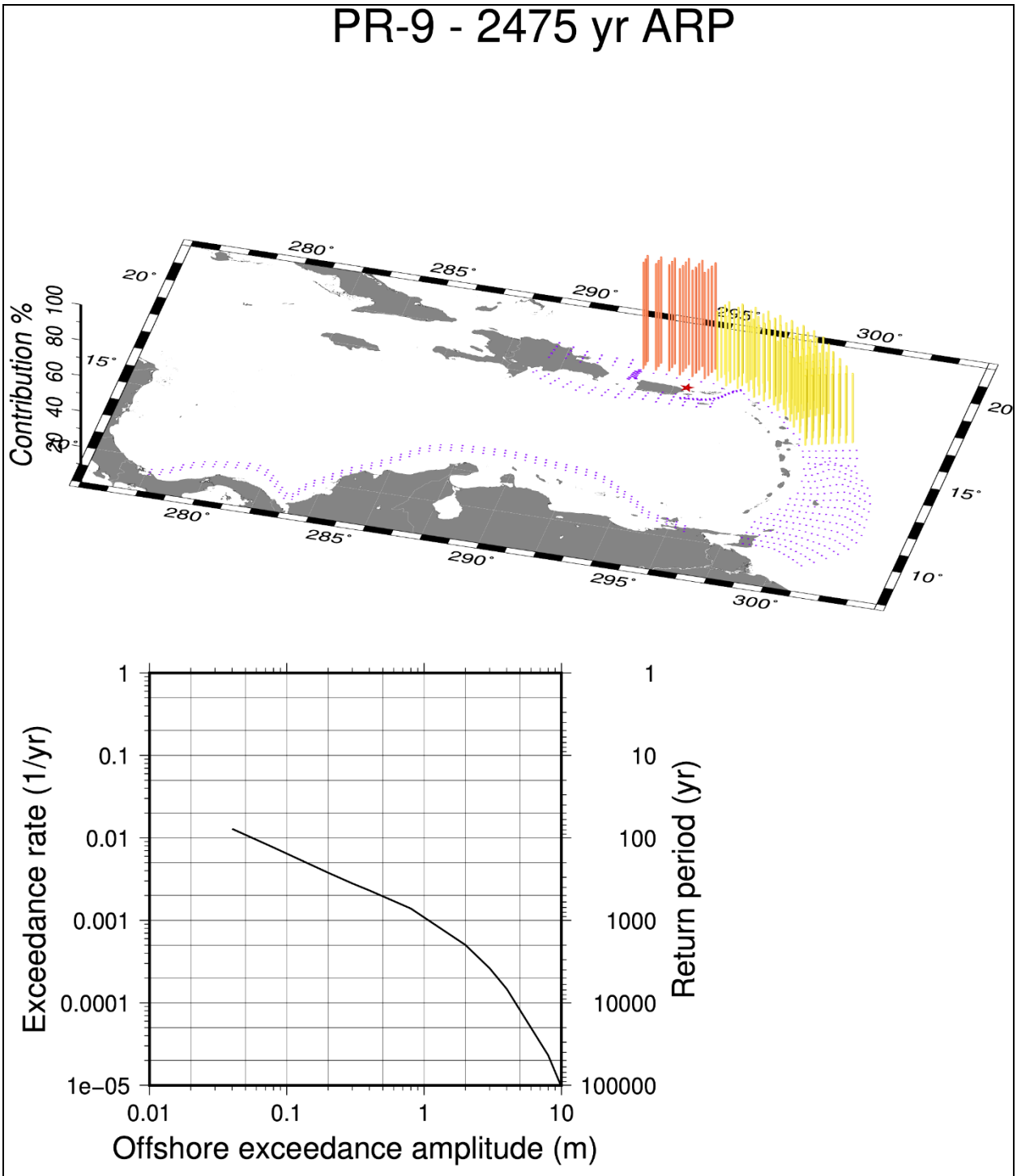

Figure B-9. Disaggregation map and hazard curve for point PR-9

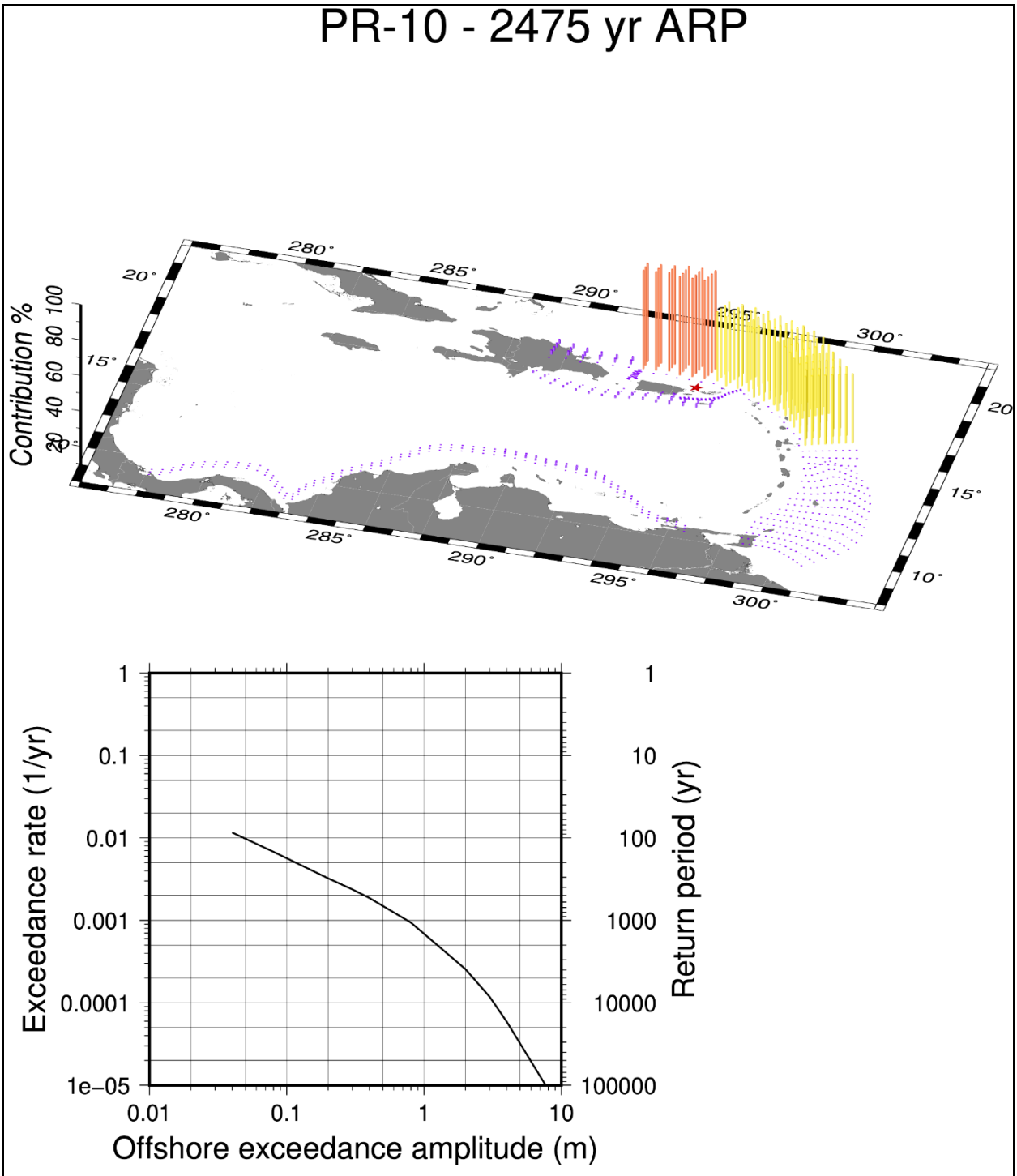

Figure B-10. Disaggregation map and hazard curve for point PR-10

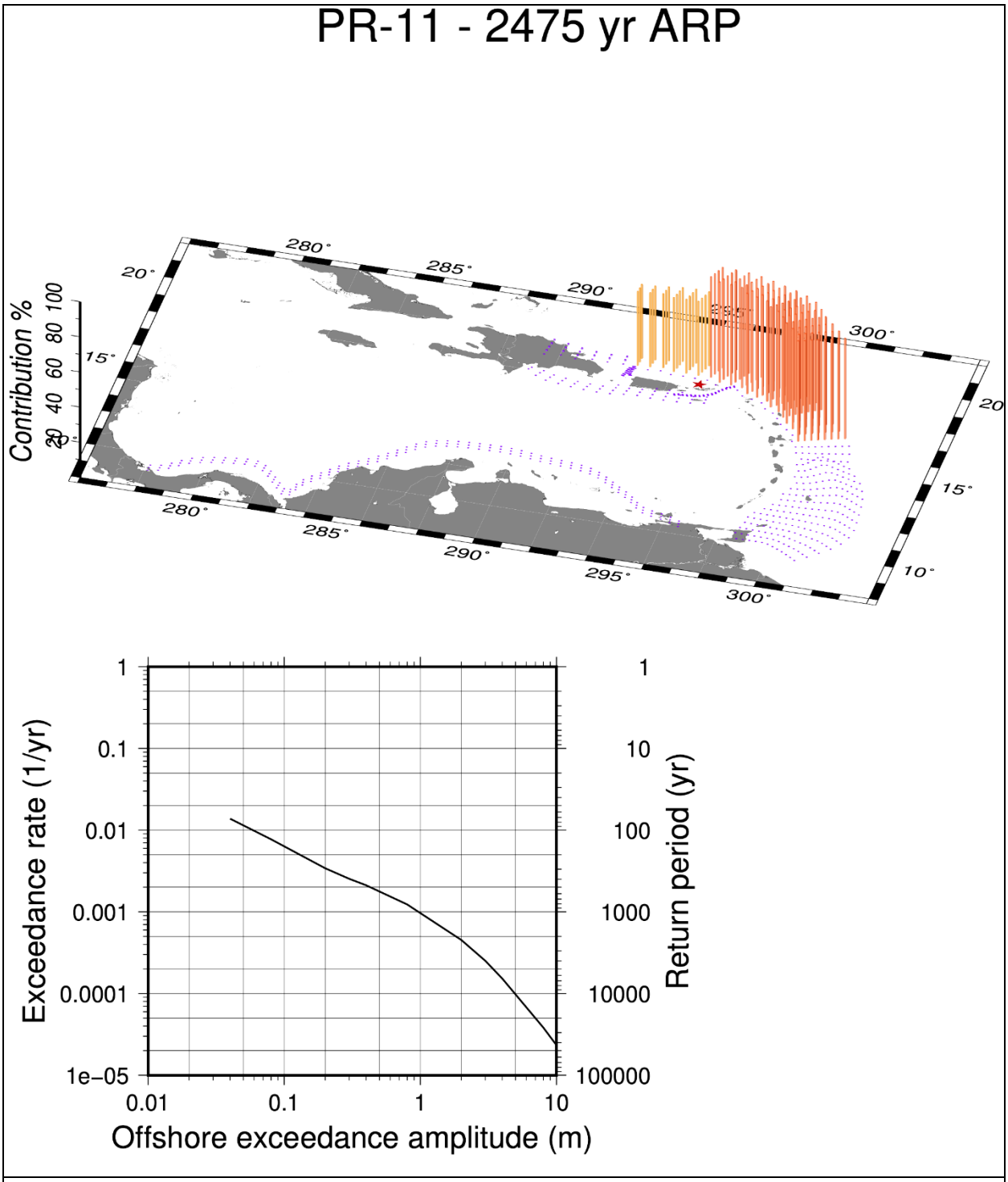

Figure B-11. Disaggregation map and hazard curve for point PR-11

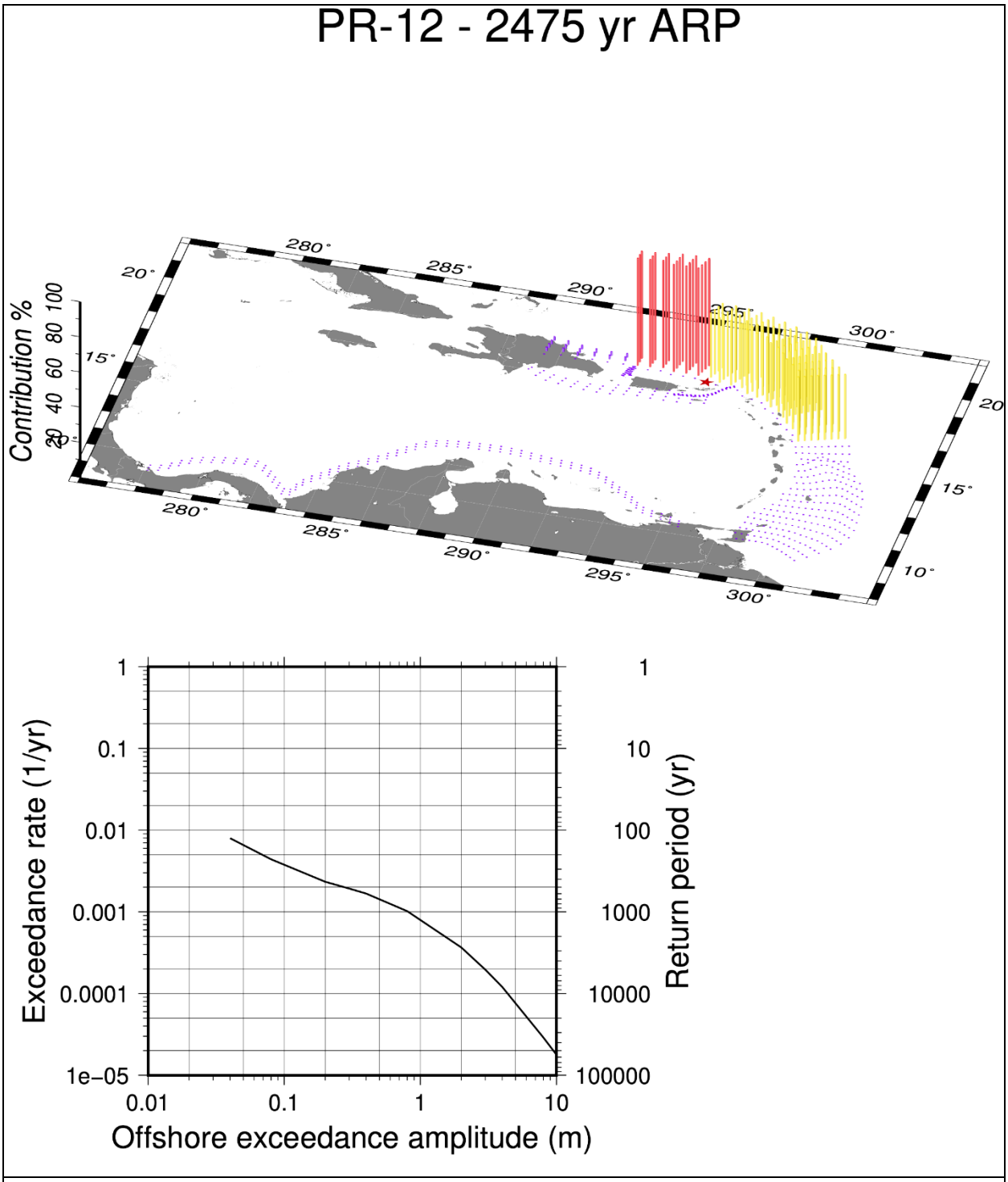

Figure B-12. Disaggregation map and hazard curve for point PR-12

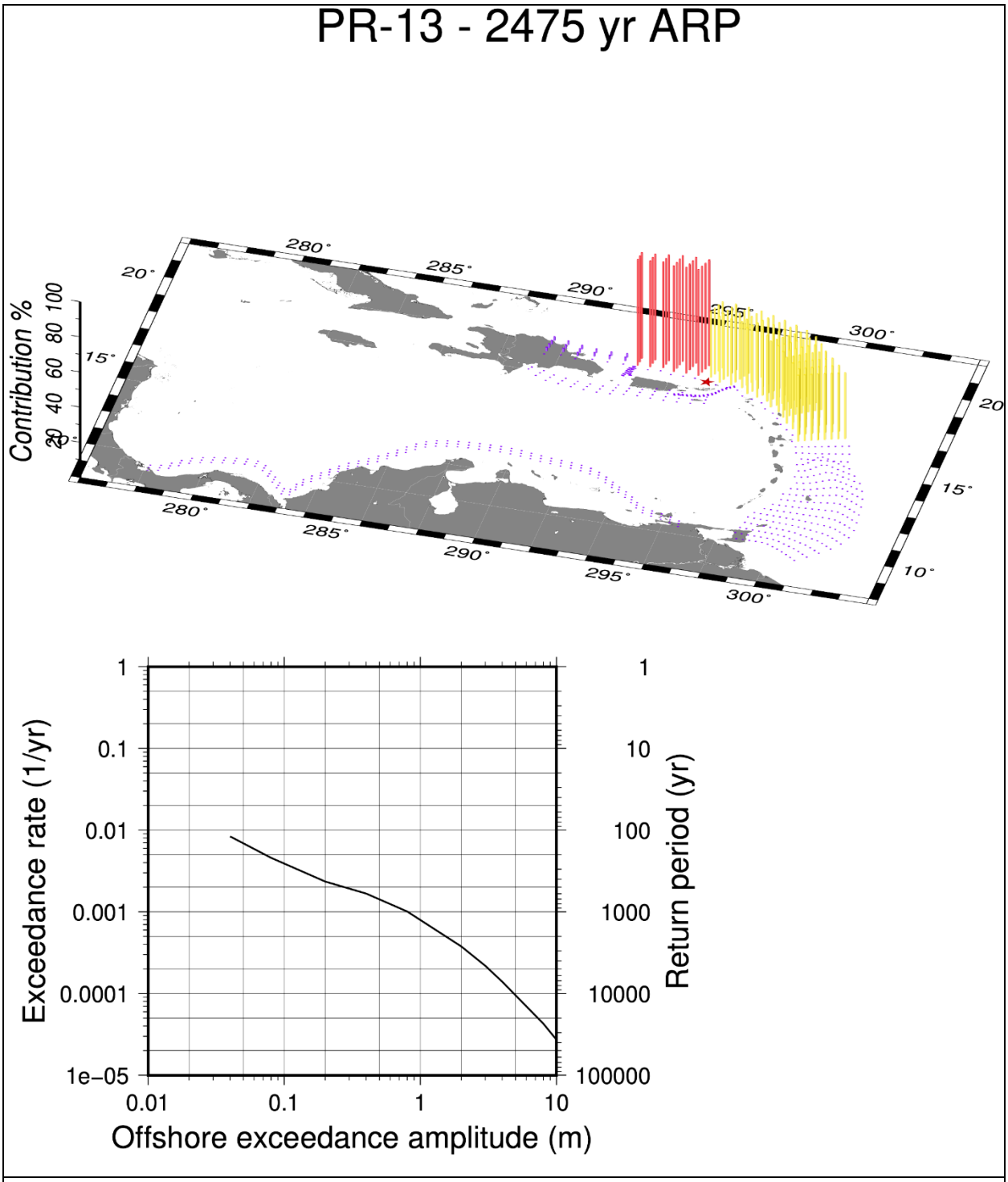

Figure B-13. Disaggregation map and hazard curve for point PR-13

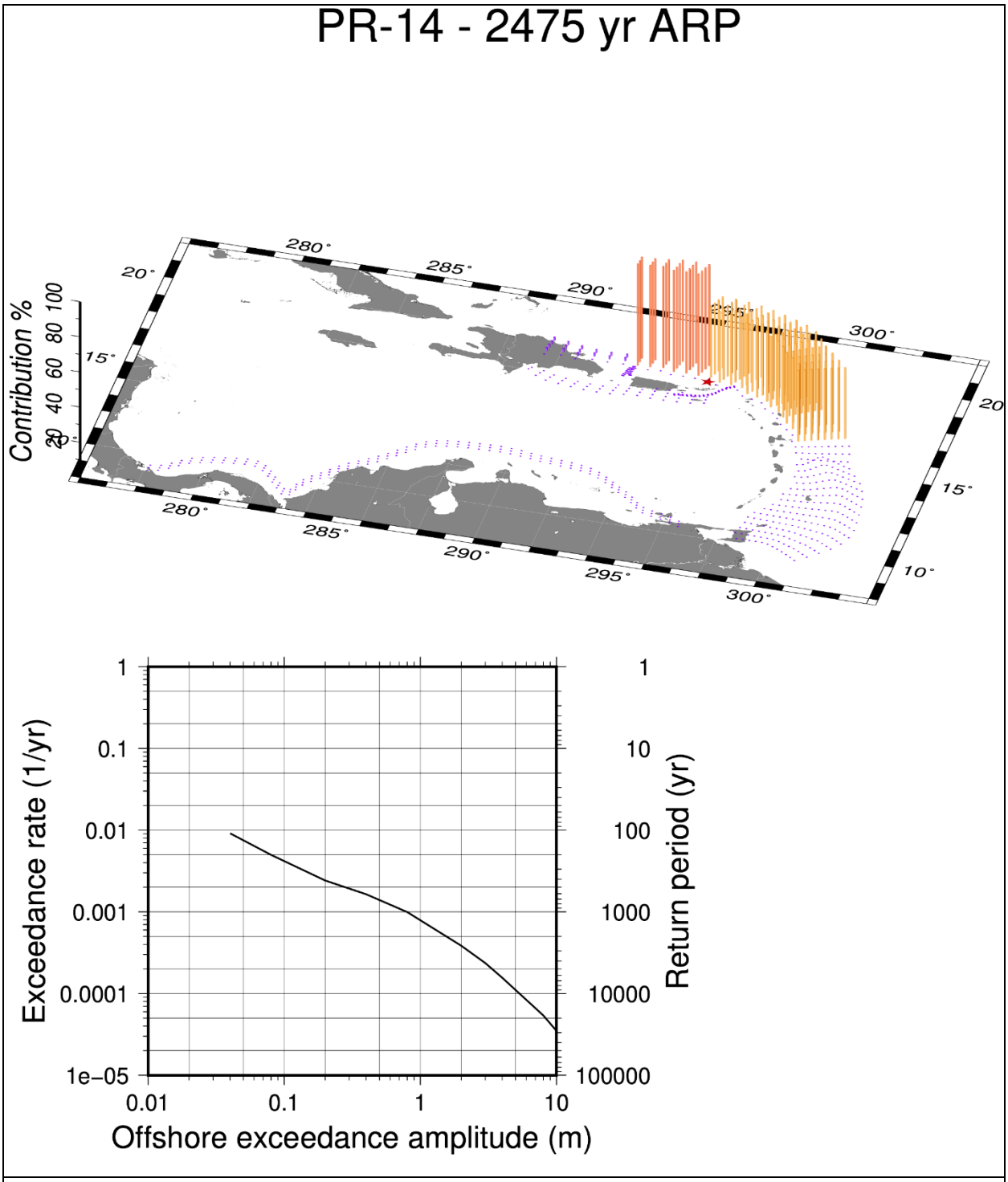

Figure B-14. Disaggregation map and hazard curve for point PR-14

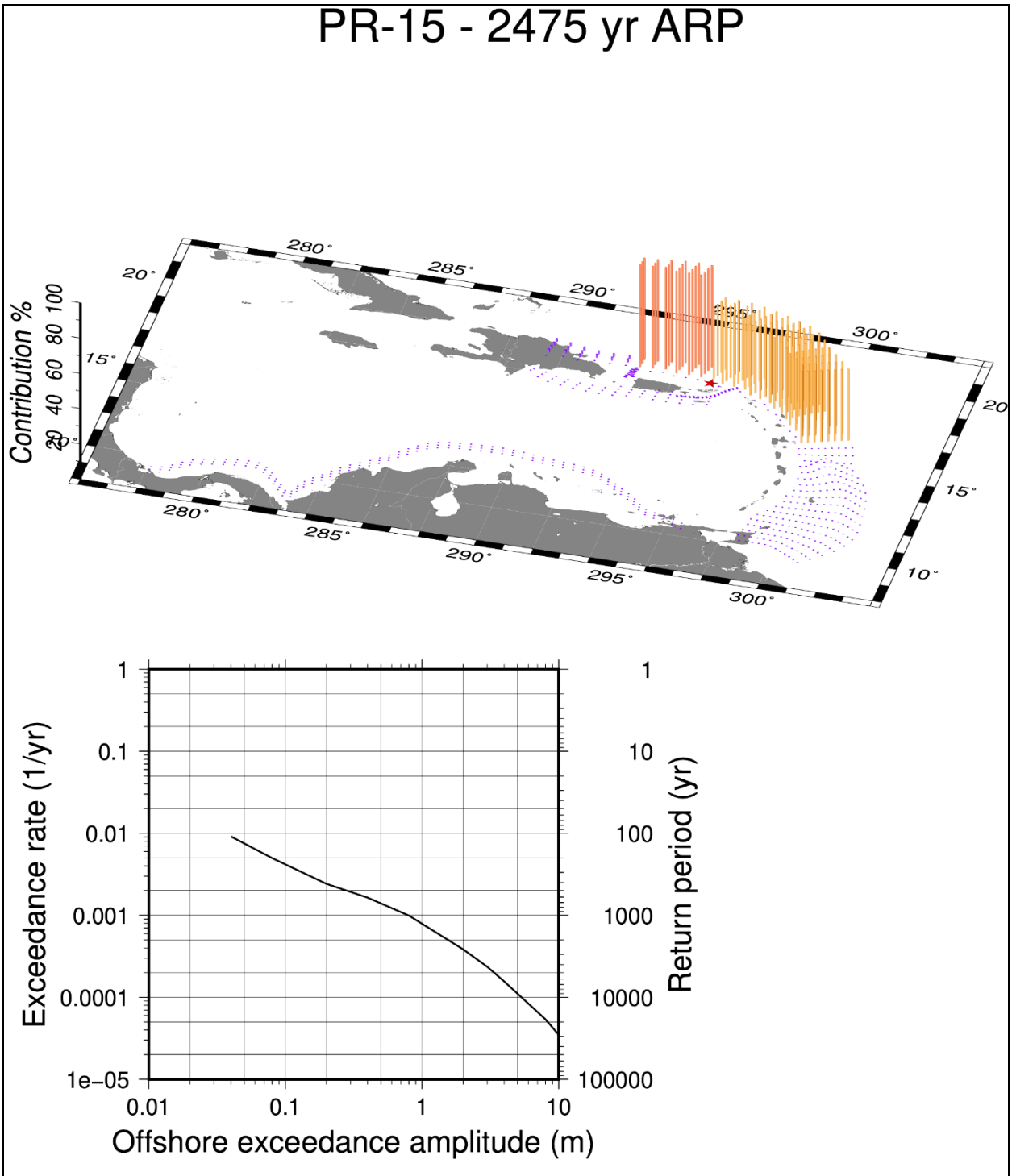

Figure B-15. Disaggregation map and hazard curve for point PR-15

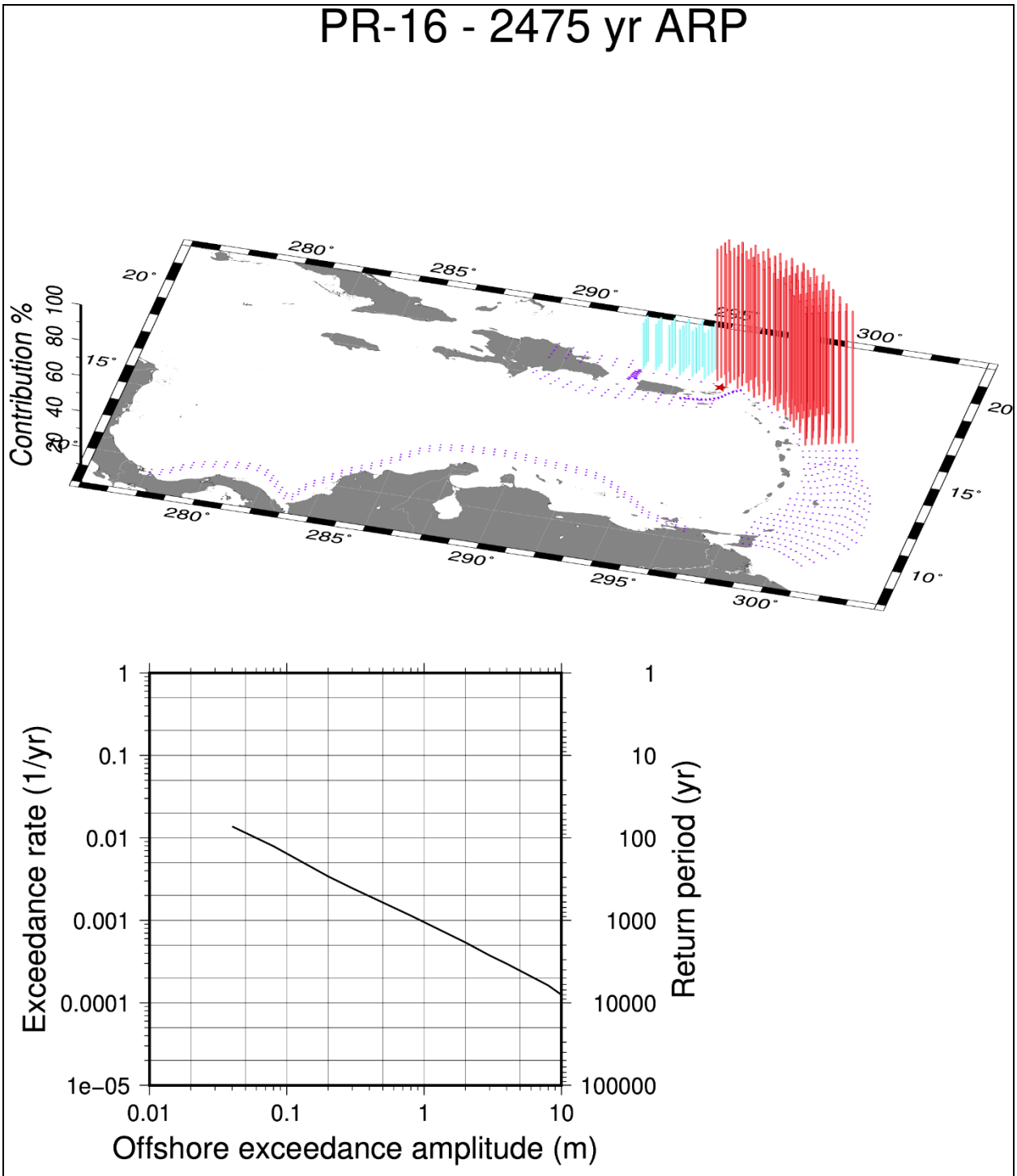

Figure B-16. Disaggregation map and hazard curve for point PR-16

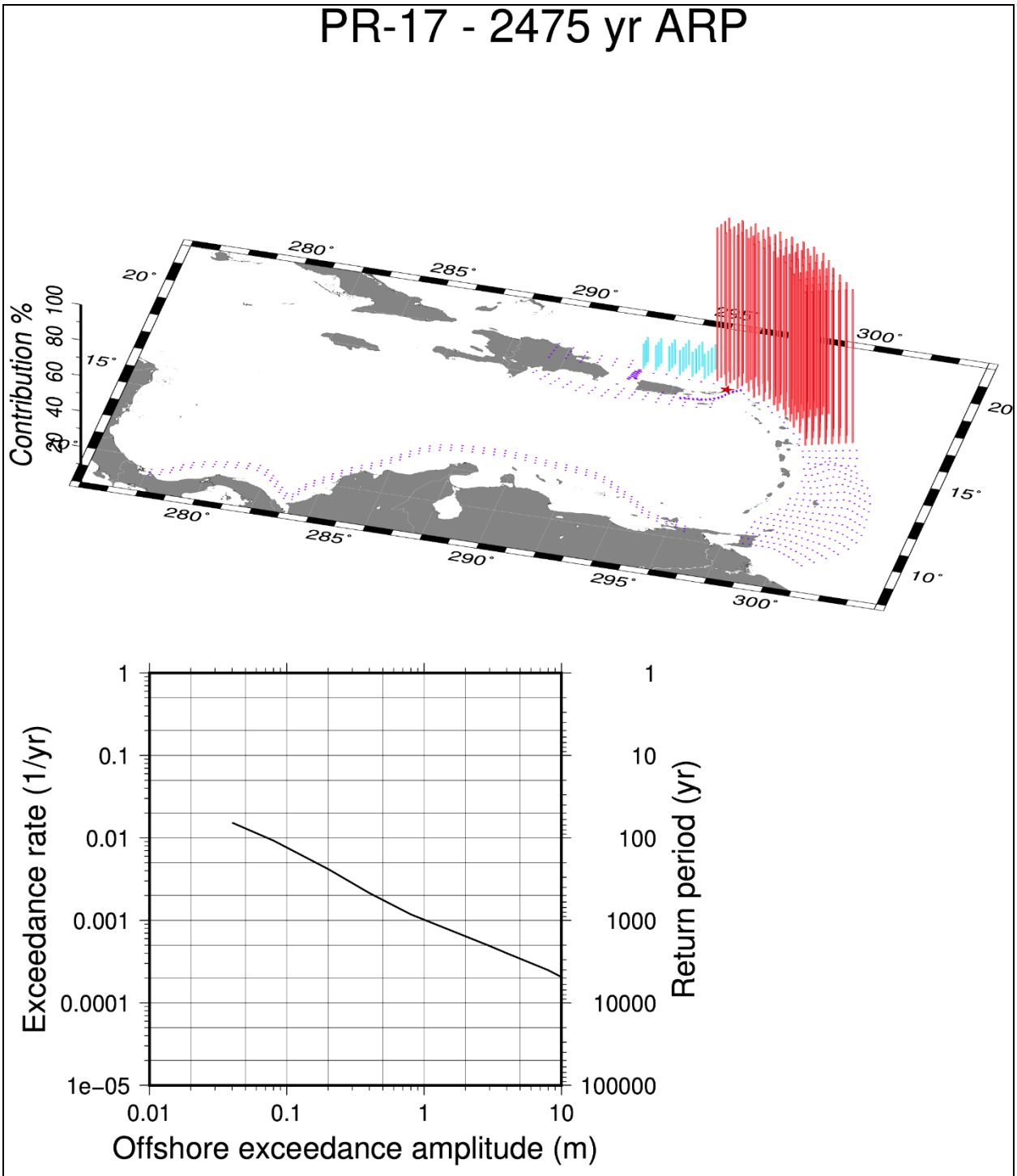

Figure B-17. Disaggregation map and hazard curve for point PR-17

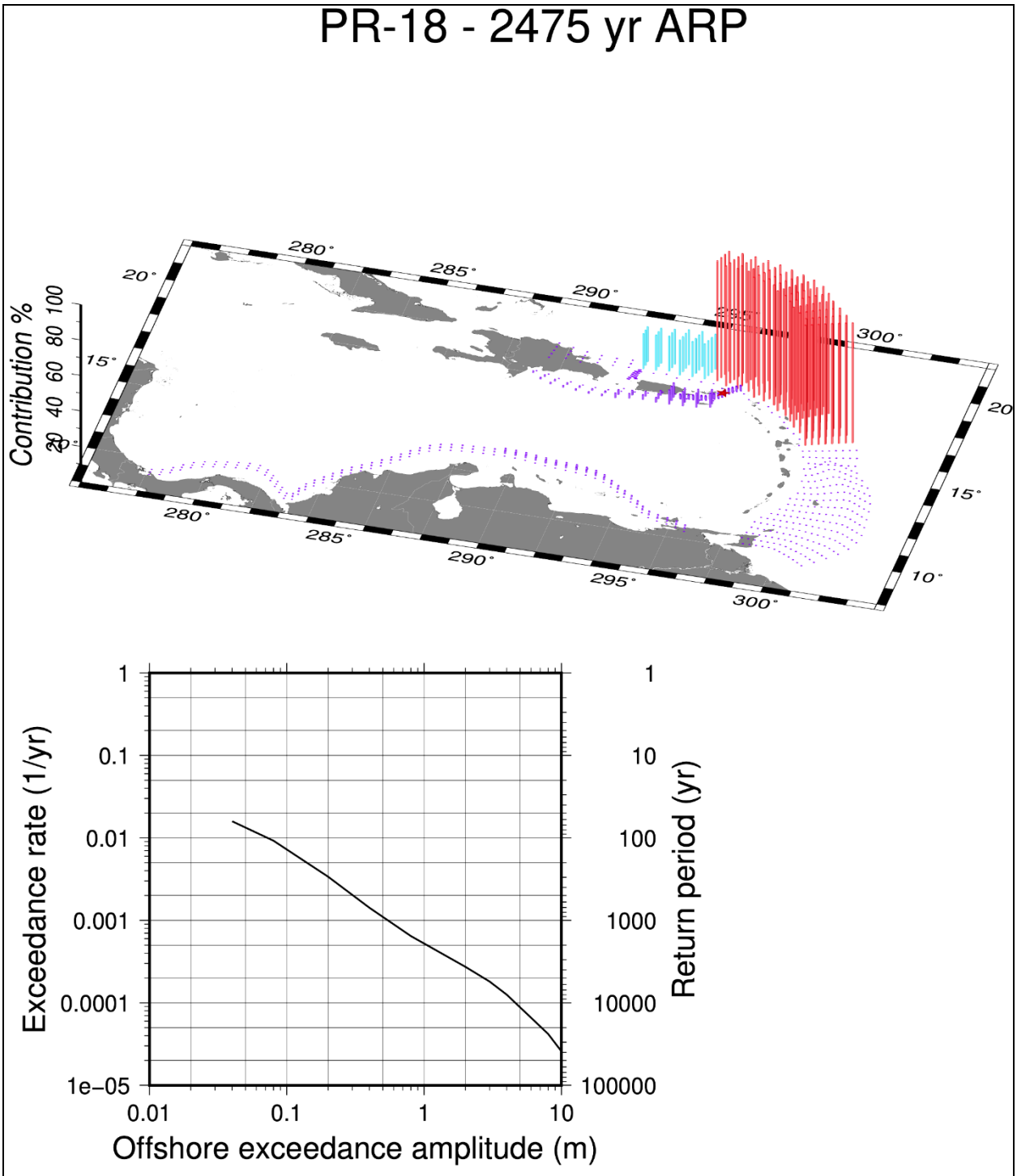

Figure B-18. Disaggregation map and hazard curve for point PR-18

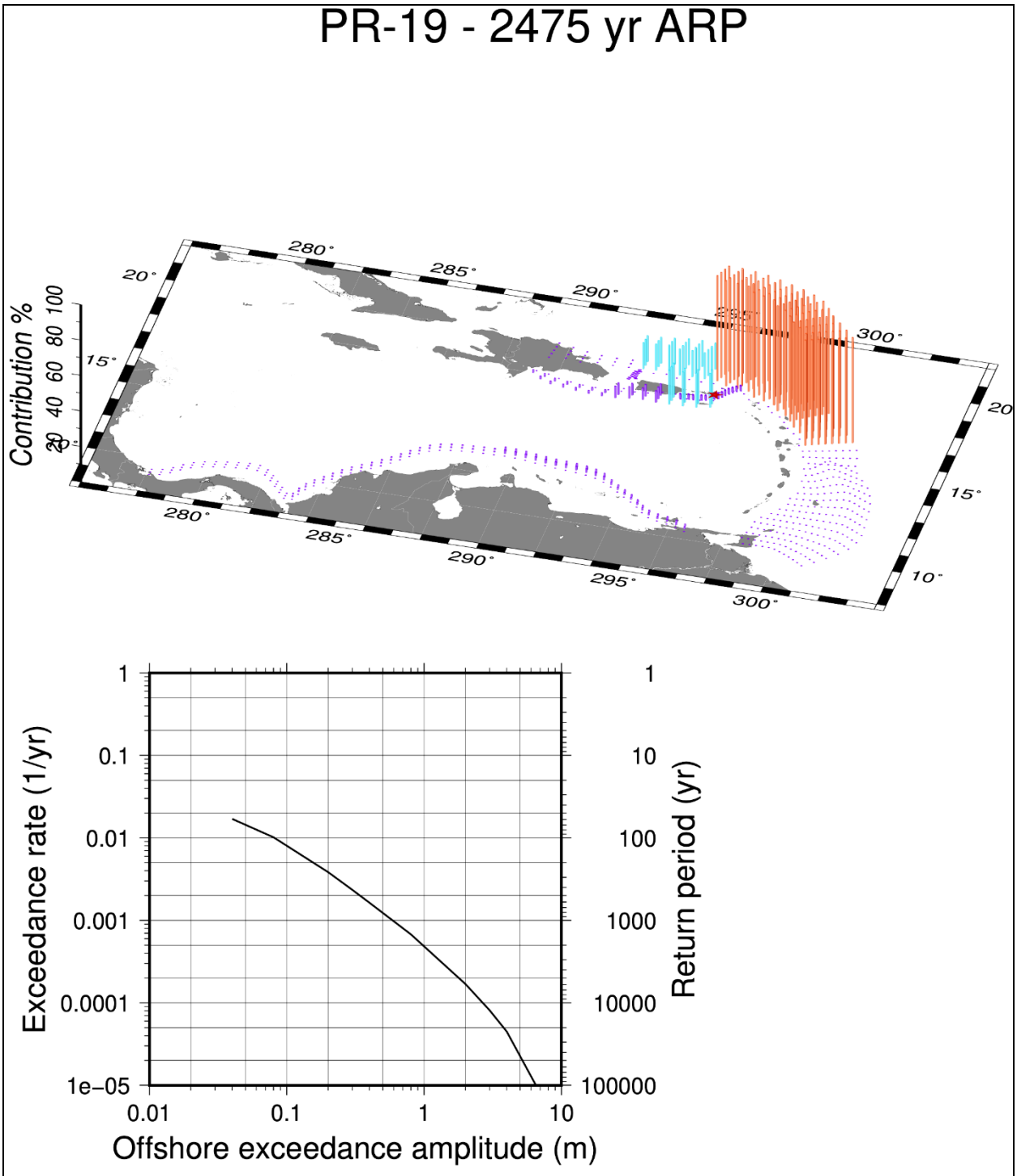

Figure B-19. Disaggregation map and hazard curve for point PR-19

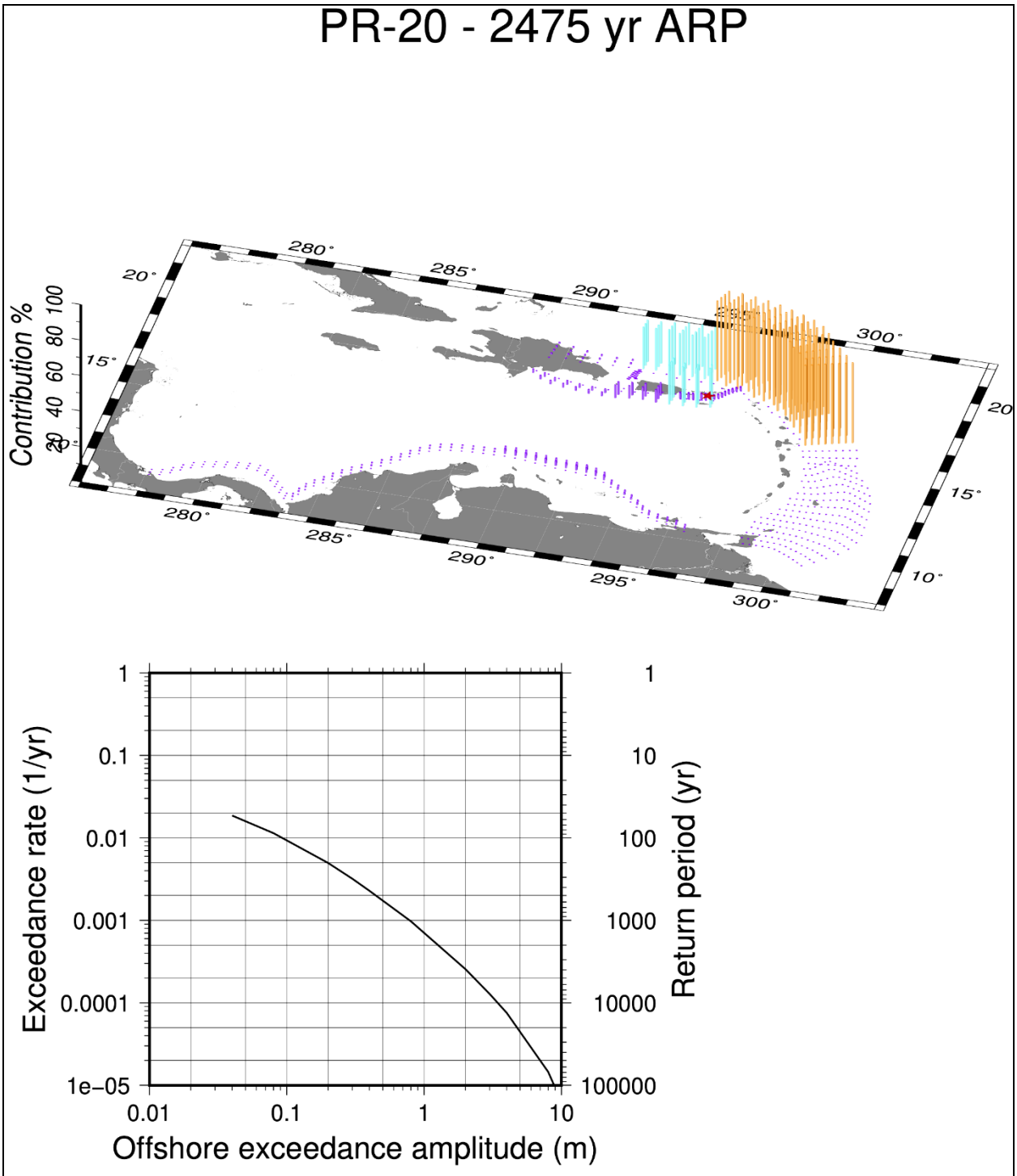

Figure B-20. Disaggregation map and hazard curve for point PR-20

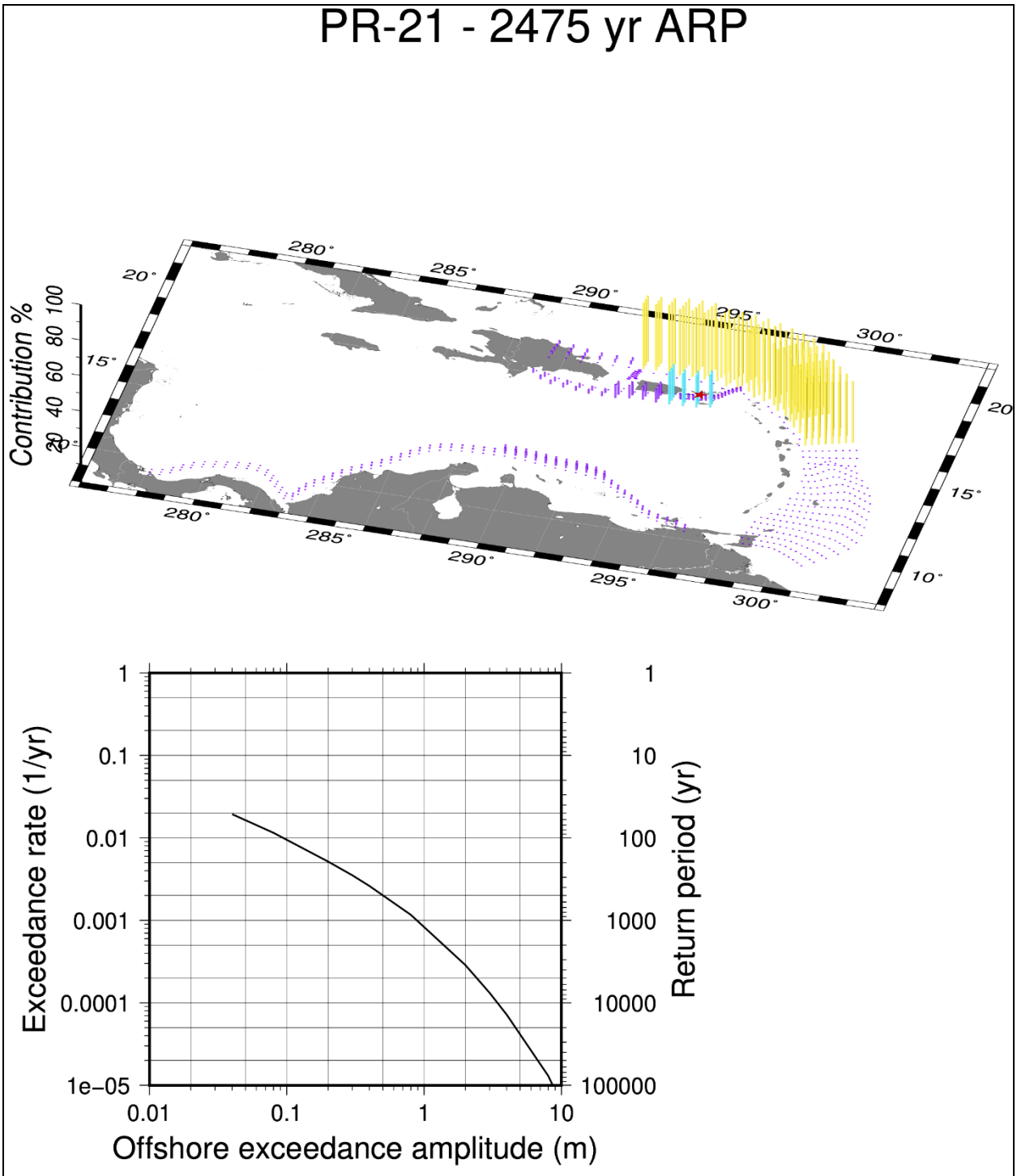

Figure B-21. Disaggregation map and hazard curve for point PR-21

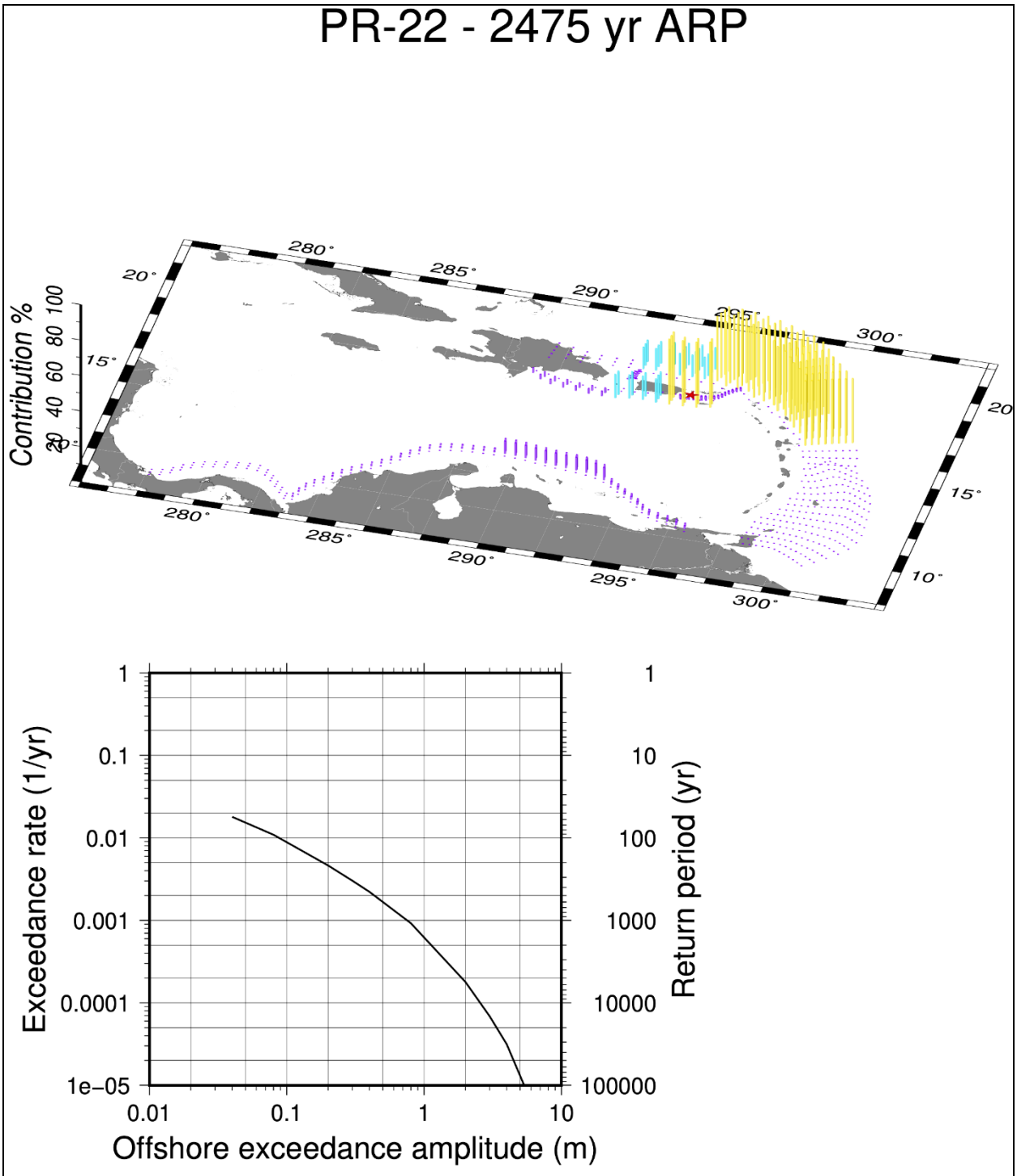

Figure B-22. Disaggregation map and hazard curve for point PR-22

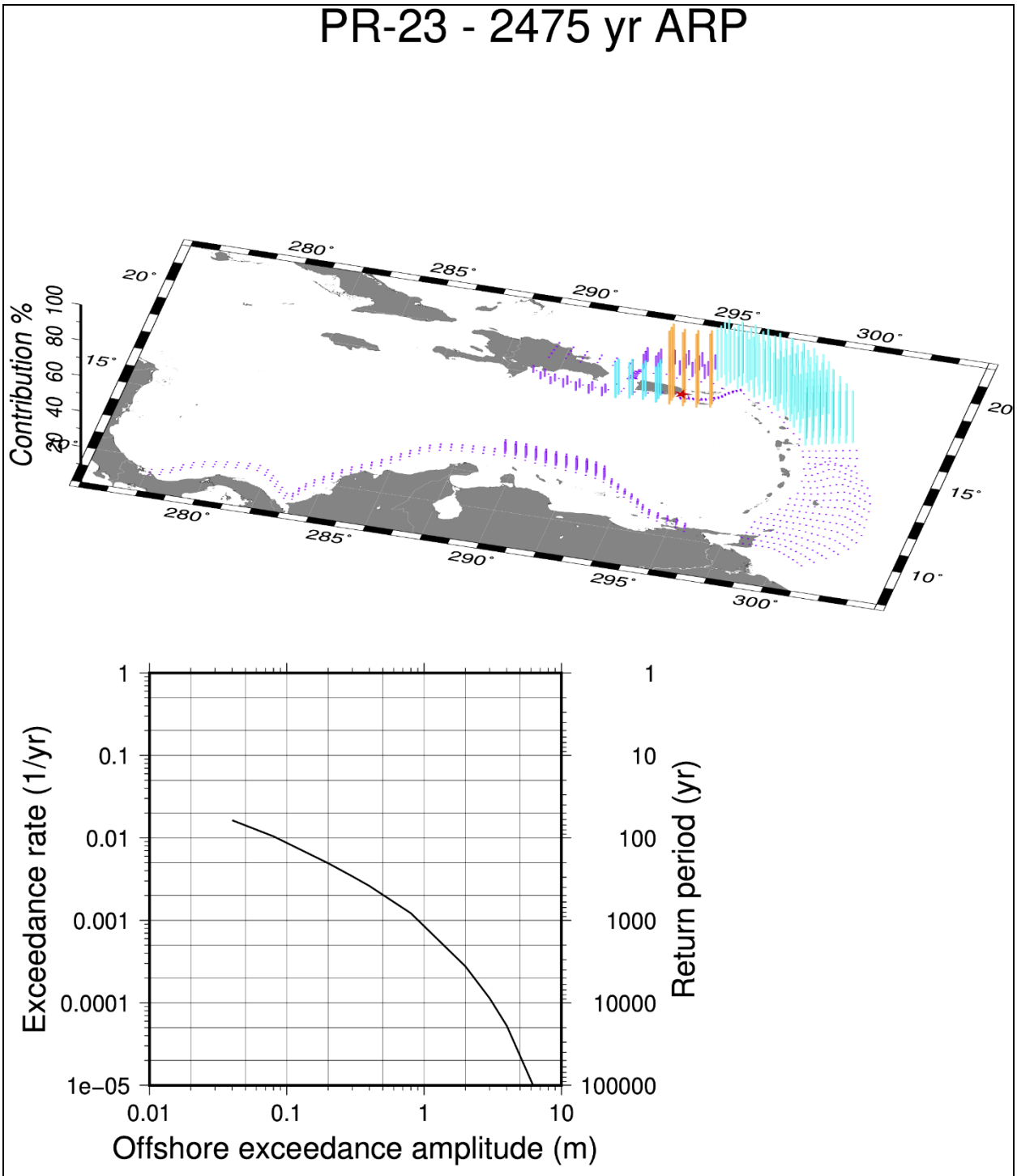

Figure B-23. Disaggregation map and hazard curve for point PR-23

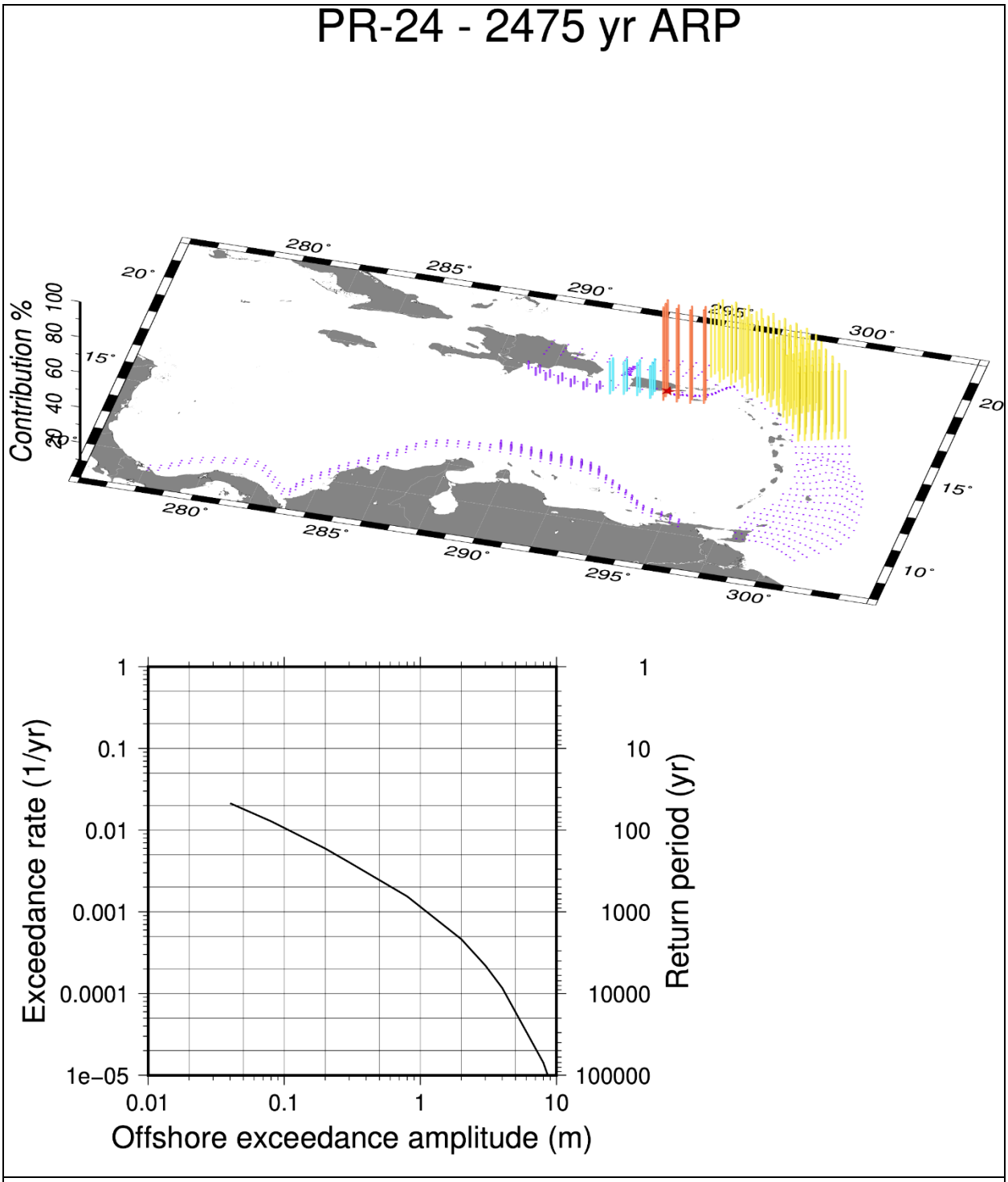

Figure B-24. Disaggregation map and hazard curve for point PR-24

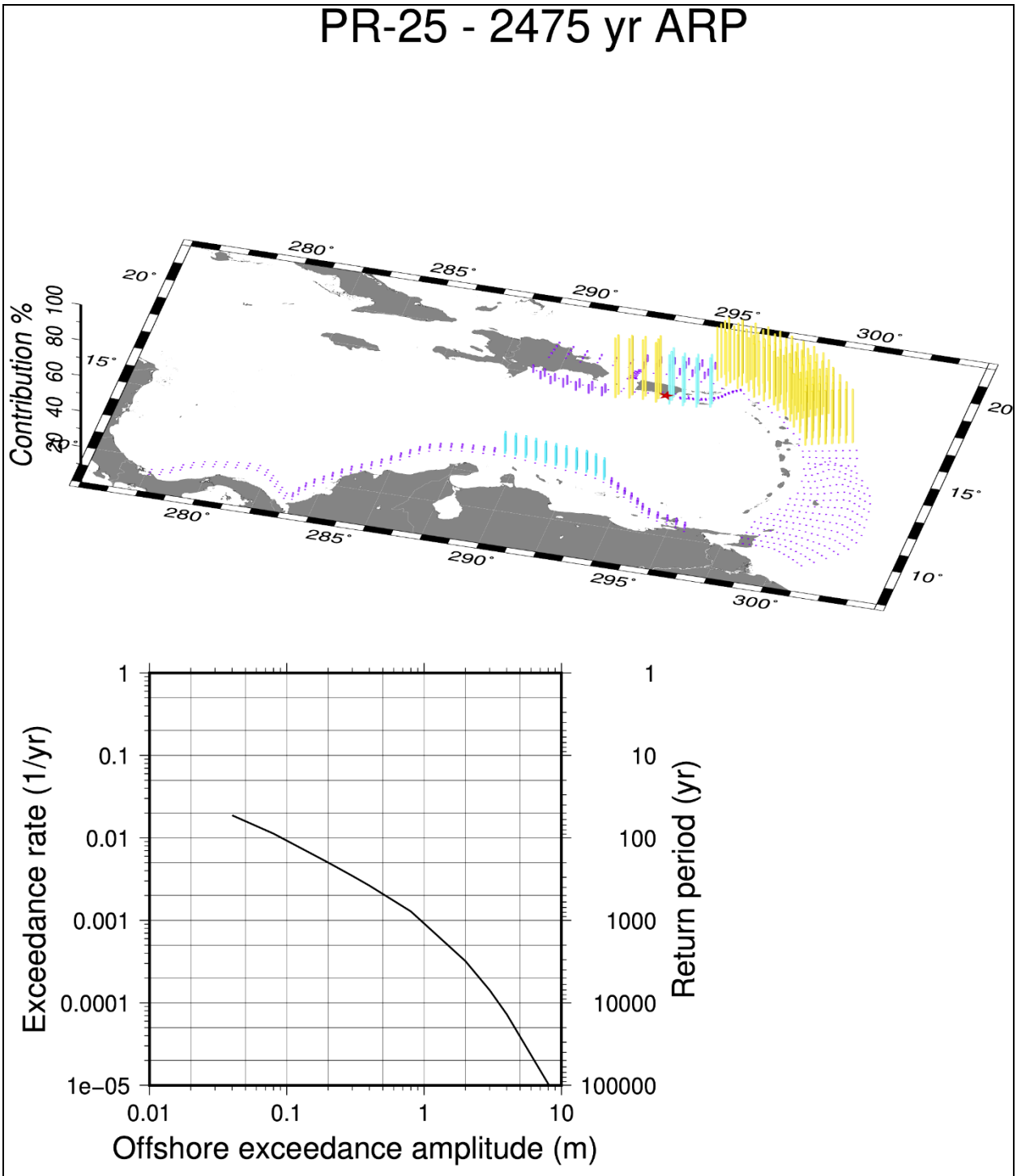

Figure B-25. Disaggregation map and hazard curve for point PR-25

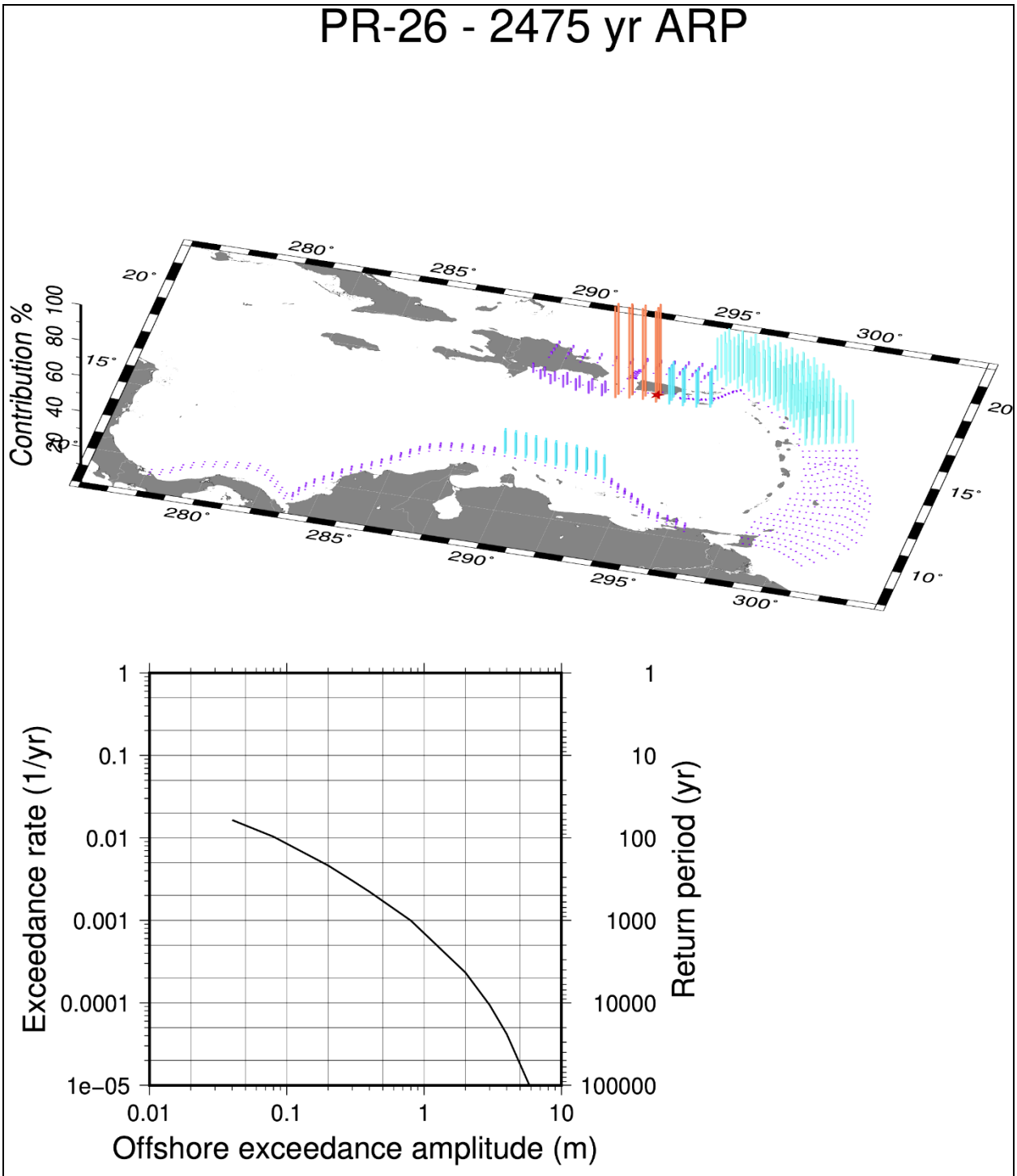

Figure B-26. Disaggregation map and hazard curve for point PR-26

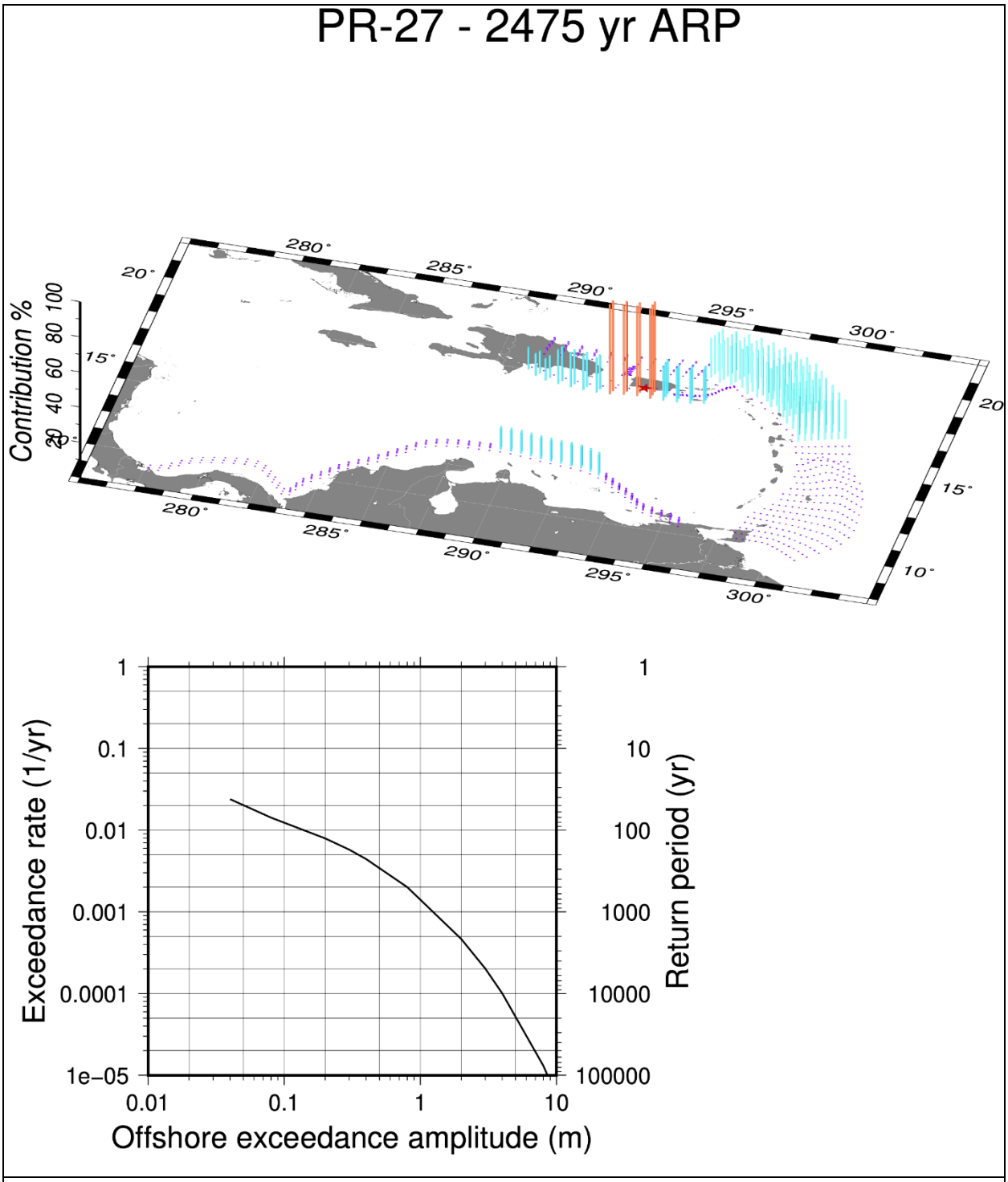

Figure B-27. Disaggregation map and hazard curve for point PR-7

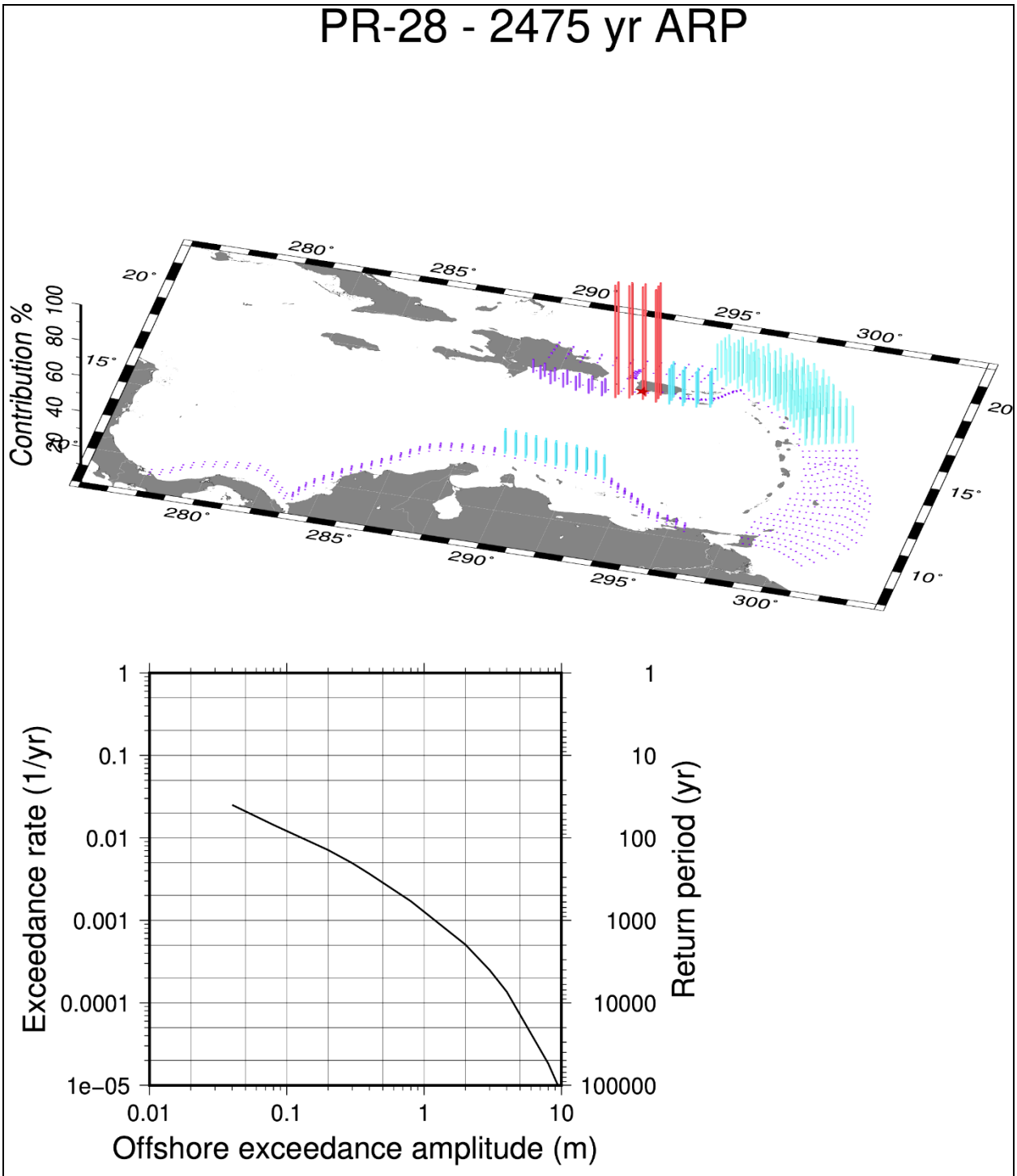

Figure B-28. Disaggregation map and hazard curve for point PR-28

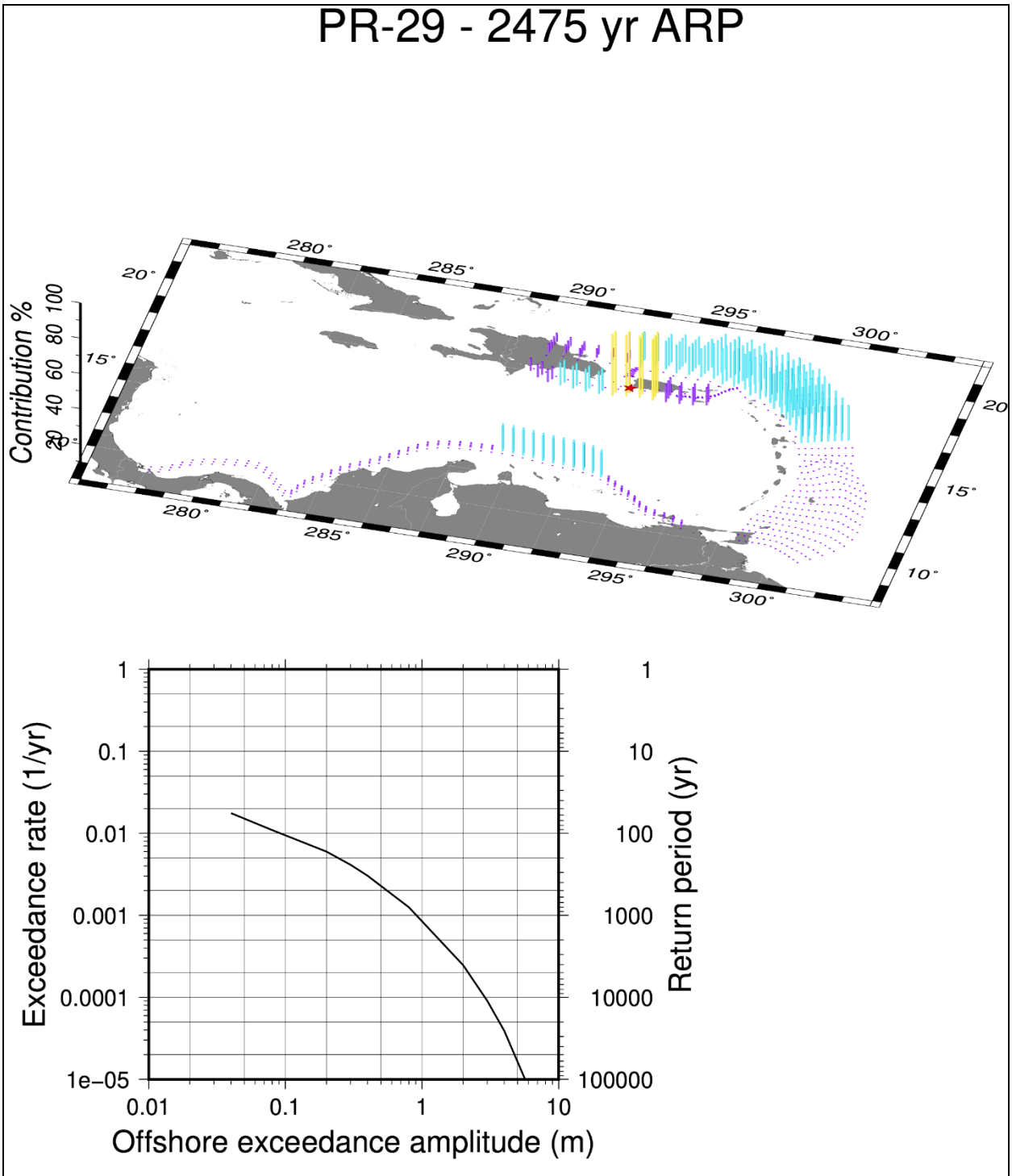

Figure B-29. Disaggregation map and hazard curve for point PR-29